WATER MASS CLASSIFICATION USING BAND RATIOS

by

RAMYA RAMADURAI

A Thesis submitted to the

Graduate School-New Brunswick

Rutgers, The State University of New Jersey

in partial fulfillment of the requirements

for the degree of

Master of Science

Graduate Program in Oceanography

written under the direction of

Scott Glenn and Oscar Schofield

and approved by

_____

_____

_____

New Brunswick, New Jersey

October, 2008

Abstract of the Thesis

Water Mass Classification Using Band Ratios

By: Ramya Ramadurai

Advisors: Scott Glenn and Oscar Schofield

The Hudson River plume has been the topic of consideration and observation in order to try and understand the physical, chemical and biological behavior of the plume which is a key component of the oceanography of the Mid-Atlantic Bight (MAB) region off the east coast of the United States. One approach towards understanding the chlorophyll production for the plume would be to make use of satellite data to measure the optical ocean color properties of these waters. In this direction classifying the water masses of the Hudson River plume according to these optical properties would be an interesting method of analyzing the satellite data for the purpose of understanding and identifying the physical and biological changes and the correlation between them in this region.

The first step is to design and implement a water mass classification algorithm in the LaTTE (Lagrangian Transport and Transformation Experiment) region of the MAB. It takes about 1-2 weeks for the nutrients from the freshwater from the Hudson Estuary to be dissipated and mixed with the open ocean. This classification algorithm is developed using ocean color data from the Sea viewing WIde Field of view Sensor (SeaWiFS). The algorithm is validated by overlaying ship salinity tracks on the classified water masses to show that salinity values change at the boundaries of the classified regions, due to the mixing and export of freshwater across the shelf.

We analyze global Sea Surface Temperature (SST) data collected over the years 1995-2005 for summer and winter in order to find coastal estuarine ecosystems that may display similar behavior as the Hudson River Estuary. Looking at the seasonal variation in this data, we observe that the regions of MAB and the East Asian coast are found to have strikingly similar seasonal behavior.

This leads into the third and the last step of the process which involves applying the water mass classification algorithm to ocean color data from eastern coastal Asia. It is observed that the algorithm well in the seas of Okhotsk, Japan and East China where it is able to identify plume water and non river water.

Acknowledgements

The research documented in this thesis was made possible by Drs. Scott Glenn and Oscar Schofield who labored incessantly to work with me in explaining and detailing the proposed technique and the primary focus of this work.

It is a matter of honor for me to have associated with Dr. Glenn, my advisor and mentor for the learning opportunity and an experience which I will cherish for the rest of my life. I would like to express my gratitude to Dr. Oscar Schofield who has constantly guided this work in adopting methods that have made our research achieve such a high quality.

Eli Hunter and John Kerfoot, research scientists in the Coastal Ocean Observation Laboratory who provided critical guidance with their rich programming skills to accomplish some of the important tasks part of this work. They also kindled my own interest in programming, which I have honed over the years I have spent here.

Dr. Jennifer Francis has over the semesters provided me with great advice flavored with intense enthusiasm which always came at the right time.

Satish E. Viswanath, a friend and so much more, for having been with me through every stage of this thesis, motivating me and encouraging me at all times. Donglai Gong, PhD student at IMCS and friend, for having painstakingly proof-read my thesis and given me invaluable feedback about things that I had missed while writing it myself.

My experience at the Institute of Marine and Coastal Sciences at Rutgers University has been a journey of self discovery, of learning and achieving and knowing that research is my destiny. I have drawn inspiration from the distinguished faculty members all of whom

have pioneered incessantly to create an academic institution which attracts the best minds from all over the world.

And last, but not least, my family for having supported me in all my endeavors.

Table of Contents

List of Tables

List of Illustrations

Introduction

For years, oceanographers have been trying to understand the dynamics of the Hudson River plume to improve our knowledge of the processes that affect the physical and biological processes in the Mid-Atlantic Region (Levinton, Waldman 2006). These studies highlight the need for long-term studies to distinguish natural from anthropogenic changes in the environment. Attempts have been made in this direction to quantify various parameters defining the Hudson River waters. The 2 largest organic carbon inputs into the Hudson are: runoff from the upper watershed (26.8%) and sewage (23.5%) (Limburg, Moran & McDowell 1986). The Hudson River estuary transports nutrients to the inner shelf, which in turn supports high phytoplankton and zooplankton production. Due to this high across-shelf nutrient transport, it also happens to be one of the most polluted estuarine systems (Levinton, Waldman 2006). Understanding the productivity trends observed in this region can give us a very good idea about the influence of human factors on primary production in an estuarine coastal system.

The traditional method of observing and measuring productivity conducted by sustained efforts on expeditionary research vessels has been increasingly expanded and enhanced by operational oceanographic methods (Barnard, Zaneveld, J. Ronald V. & Pegau 1999, Kidder, Vonder Haar 1995, Schofield et al. 2004b). The use of satellite technology and remote sensing methods has proved very useful in ocean color and sea surface temperature measurements among others. Satellite remote sensing helps in covering a larger area than field measurements and has proven to be much less expensive than shipboard measurements (Kidder, Vonder Haar 1995).

Due to the nutrient pollution and its consequent influences on productivity there (Levinton, Waldman 2006), it is useful to classify the Hudson River water based on productivity for better understanding of the turbid waters of the plume (Johnson, Miller & Schofield 2003). Due to the ready availability of satellite generated data (Alvaina et al. 2005, McClain, Feldman & Hooker 2004)() for the Hudson River plume, it is easy to process the data and work out techniques to classify these waters.

Another matter worthy of consideration is that of behavioral similarities between the Hudson River plume and other estuarine coastal systems around the world. One way of estimating these similarities is by using global SST data and looking for similar trends in other coastal ecosystems. Once these similarities have been identified techniques developed for the MAB can be taken to a global scale and applied to such similar regions. This, in fact forms the final step of this thesis in which we look at ocean color in similar SST regimes around the world.

Thus, this technique helps us answer some fundamental questions such as how water masses can be distinctly identified based on their constituent components, whether global satellite data analysis yields a solid ground for comparison between different estuarine ecosystems and whether techniques applicable to one region can be tweaked to work in other regions, thus helping us develop one standard universal model that can fit the waters of the world over.

The Hudson River Estuary

The Hudson River Estuary is one of the most productive shelf ecosystems on Earth (O'Reilly, Busch 1984) . It is characterized by relatively high mean chlorophyll-a values (3-5 mg/m^{-3}) throughout the year with peak values found in late winter and early spring as the shelf waters begin to stratify. Productivity values tend to be lowest during the highly stratified summer season when nutrients are low on the shelf. Superimposed on this is the productivity associated with rivers and summertime nearshore coastal upwelling (Glenn et al. 2004).

The horizontal transport of the freshwater as well as the stratification in the Hudson estuary is governed by spring and neap tides. During neap tides, vertical gradients being strong, there is minimal vertical exchange of salt, thus enhancing stratification and estuarine circulation. This causes salt to advance into the estuary during spring tides and retreat during neap tides. Thus the lateral mixing processes follow fortnightly variations, causing pronounced variations in the estuarine regime (Levinton, Waldman 2006). This means that the time period required for freshwater to become well mixed with the coastal shelf water is about 2 weeks.

Seasonal coastal upwelling in the Hudson estuary normally occurs during the summer months because of alongshore wind episodes (Glenn et al. 1996). An onshore deeper flow that brings colder and nutrient-rich water to the surface becomes instrumental in cross-shelf nutrient exchanges. Despite the relatively low outflow of the Hudson River it provides a disproportionately large contribution to the MAB productivity (Levinton, Waldman 2006).

The two largest organic carbon inputs into the Hudson are runoff from the upper watershed (26.8%) and sewage (23.5%) (Limburg, Moran & McDowell 1986). The Hudson River estuary transports nutrients to the inner shelf, which in turn supports high phytoplankton and zooplankton production. Due to this high across-shelf nutrient transport, the river also happens to be one of the most polluted estuarine systems (Levinton, Waldman 2006).

Primary productivity in the saline Hudson River estuary is strongly regulated by nutrient loading and concentrations, which are indirectly dependent on the residence times in the estuary. Phytoplankton production is enhanced at the shelf break during the stratified season when shelf water transported offshore is upwelled along frontal isopycnals during periods of stratification as well as those of intense mixing (Ryan, Yoder & Cornillon 1999). The spring bloom of phytoplankton occurs during the upwelling period of March-April during which our study was conducted (Siegel, Doney & Yoder 2002).

The East Asian Coast

The East Asian coast relevant to this thesis comprises the seas of Okhotsk, Japan (East Sea) and the Yellow Sea. These regions are all part of the 64 Large Marine Ecosystems developed by NOAA for oceanic conservation. As explained previously, these regions were chosen because of the similar latitude locations to the NJ shelf which implies similar spatio-temporal SST variations. They are also estuarine systems, in that they have river outflow, which was successfully identified by the water mass tagging algorithm. In addition to this, they are all influenced by western boundary currents, which give us additional motivation to apply the water mass tagging technique to these waters.

The Sea of Okhotsk: (Most parts of this section reference (Alekseev et al. 2006, Dulepova, Radchenko))

Fig. 2 shows the physical boundaries of the Sea of Okhotsk. It is the northernmost sea in our area of interest. The Okhotsk Sea is situated at the margin of the northwestern Pacific Ocean between 43°43' and 62°42' N, and 135°10' and 164°54' E. It is separated from the open ocean by the chain of the Kuril Islands and the Kamchatka Peninsula.

The Okhotsk Sea sub-system is located within the monsoon climatic zone of the moderate latitudes. The northern region of the Sea is strongly influenced by the Arctic climate. Average annual temperatures range from 5 to 7°C. The generally monsoonal climatic conditions are often disturbed by cyclones which traverse the region from southwest to northeast. The summer is characterized by high precipitation rates, whereas the spring and autumn seasons are short, cold and cloudy. The winter, particularly in the northern region, is long and severe, with frequent wind and snowstorms. The major currents in the region include the Penzhinskoye, Yamskoye, North-Okhotsk currents and counter-currents, and the East-Sakhalin, Middle and Soya currents (Dulepova, Radchenko).

A regular supply of nutrients in the area results mainly from river runoff. The riverine flow permanently supplies the photosynthetic zone with nutrients. Due to the internal recycling of nutrients, a high level of phytoplankton biomass can be observed following the spring bloom. An estimated seasonal relative share of primary production is 35% in spring, 45% in summer, 18% in autumn, and 2% in winter (Alekseev et al. 2006).

The Yellow Sea: (Most parts of this section reference (NOAA 2003, Teng et al. 2005))

The Yellow Sea (Fig. 4) is also a semi-enclosed body of water bordering the Chinese mainland to the west and Korea to the east. It is connected to the Bohai Sea to the north and to the East China Sea in the south, thus forming a continuous circulation system among these three seas. Its spatial extents are approximately 33° to 40° N and 123° to 126° E.

The central part of the Yellow Sea is called the Yellow Sea Basin and is the major over-wintering ground for fish and invertebrates. The water mass in the Yellow Sea is in continuous circulation with those of the Bohai Sea and the East China Sea. A branch of the Tsushima Warm Current from the Kuroshio Current, which comes from the East China Sea, carries relatively high salinity and high-temperature water flowing northward into the Bohai Sea in the winter. This current plays an important role in the circulation in the semi-enclosed Yellow Sea.

During winter, the surface water temperatures in the Yellow Sea may decrease to the freezing point in the northern part, but with temperatures gradually warming to the south while during summer, the water temperatures may rise to as high as 27-28° C.

The Yellow Sea receives a huge volume of sediments mainly from the Yellow (Changjiang) River on its north and Yangtze River on its south; both rivers forming large deltas at their mouths. The biotic communities of the southeastern Yellow Sea are complex in terms of their composition, distribution and structure. Yet the diversity and abundance of the fauna are comparatively low. All components of the biotic communities show marked seasonal variations. Turbidity and sediment types appear to be the major

parameters that affect the distribution of planktonic and benthic organisms in the coastal waters of the Yellow Sea.

Ocean Optics Background

Ocean optics is the branch of oceanography that deals with the behavior of light in natural waters. Light refers to the radiation in the electromagnetic spectrum (about 400 – 700 nm) that is visible to the human eye. Coincidentally, aquatic photosynthesis also occurs within this waveband, which makes it possible for satellite ocean color sensors to identify phytoplankton biomass, based on ocean optics.

Light within water can be either absorbed or scattered. The absorption and scattering properties of the aquatic medium for light of any given wavelength can be measured in terms of the absorption coefficient, the scattering coefficient and the volume scattering function. These are referred to as inherent optical properties (IOPs) (Kirk 1994). The light emanating from the ocean in every wavelength is the result of absorption and scattering in that wavelength. Absorption removes light and scattering ultimately redirects the light from its downward path (from the incident solar beam) into an upward path (Kidder, Vonder Haar 1995). Water-leaving radiance is the radiance that is backscattered out of the water and subsequently propagates to the top of the atmosphere (Yentsch 1984). Eighty to ninety per cent of the radiance received by a satellite is due to atmospheric effects. The remaining 10-20% is the radiance that ultimately leaves the ocean surface as water-leaving radiance (Kidder, Vonder Haar 1995). Applying atmospheric correction algorithms (Gordon, Wang 1993) can aid in retrieval of the water-leaving radiance from the radiance observed by the sensor.

There are many components of a medium that absorb light and many components that scatter light and so the amount of radiance is dependent upon the relative concentrations

of each component quantity. The total IOPs of a body of seawater can be considered as the sum of the partial contributions from water itself and a number of optically significant constituents. These constituents are generally divided into four classes: phytoplankton cells and colonies; mineral suspended solids; colored (or chromomorphic) dissolved organic matter (CDOM); organic suspended solids or detritus. The concentration of the photosynthetic pigment chlorophyll a is often used as a proxy variable for phytoplankton biomass. Mineral particle and organic detritus concentrations are determined by filtering water samples through a fine glass fiber filter and measuring the dry weight of material retained before and after combusting the filter at 500°C to remove the organic portion. Since there is no standard method for measuring the mass concentration of CDOM, it is conventionally measured as the absorption coefficient at 440 nm of seawater which has been passed through a membrane filter with a 0.2 μm pore size (Kirk 1994).

The two fundamental assumptions here are (1) the absorption and scattering properties are conservative, i.e. the total absorption (or scattering) is equal to the sum of the absorption (or scattering) properties of each component, and (2) the absorption and scattering properties are linearly related to the concentration of the component, i.e., the absorption by phytoplankton is proportional to the concentration of phytoplankton.

It is observed that there is a correlation between phytoplankton concentration and the red (670 nm) reflectance. Chlorophyll absorption peaks in the 670 nm reflectance, while phytoplankton biomass reflectance peaks in the near-infrared (700 nm) region. Similarly, there is a correlation between CDOM and the blue reflectance bands. CDOM absorption increases with decreasing wavelength and is much greater at 412 nm than at 443 nm. At the same time, reflectance values at 490 nm are used to estimate effects of backscattering.

Hence in order to calculate the relative contribution of CDOM, the normalized water-leaving radiance at 490 nm was used to calculate band ratios (Kirk 1994). This can be seen in the absorption spectra shown in (Fig. 1).

For absorption, a:

$$a_{total}(\lambda) = a_{water}(\lambda) + a_{phytoplankton}(\lambda) + a_{CDOM}(\lambda) + a_{non\text{-}algal\ particles}(\lambda)$$

Each component has a characteristic spectrum with respect to wavelength (λ). Water is generally low in the 400 – 500 nm or blue channel (scattering) and very high in the 600 – 700 nm red channel (absorption). Phytoplankton have two peaks associated with chlorophyll a at 436 nm and 676 nm with broad shoulders in between associated with their accessory pigments. Both non-algal particles and CDOM absorb strongly in the blue region of the spectrum and that absorption decays exponentially with depth although the slope of the decay s steeper for CDOM than for non-algal particles (Kirk 1994, Roesler, Perry & Carder 1989) (Refer Fig. 1). Radiances are dependent upon backscattering and small particles which scatter largely in the blue are more efficient backscatterers than are large particles (Morel, Bricaud 1981). So, for scattering b:

$$b_{total}(\lambda) = b_{water}(\lambda) + b_{phytoplankton}(\lambda) + b_{CDOM}(\lambda) + b_{non\text{-}algal\ particles}(\lambda)$$

and backscattering b_b:

$$b_{b\text{-}total}(\lambda) = b_{b\text{-}water}(\lambda) + b_{b\text{-}particles}(\lambda)$$

where the wavelength dependence of $b_{b\text{-}particles}$ and the ratio of $b_b(\lambda)/ b(\lambda)$ are both size dependent. The water-leaving radiance is a function of these optical properties (Morel

1973). The reflectance spectrum can thus be used to obtain estimates of each component, which is what the band ratios are intended to do (Roesler, Perry 1995).

Related Work

Hydrological optics can play a very important role in physical, chemical and biological oceanography (Schofield et al. 2004a). The ability to map the color of the world's oceans has been used to estimate global ocean productivity which aid in understanding radiant heating processes. The earliest ocean color imager was the Coastal Zone Color Scanner (CZCS) which opened up whole new avenues for understanding the global ocean primary production (Hovis et al. 1980, Hovis et al. 1980). A large data set containing coincident in situ chlorophyll and remote sensing reflectance measurements was used to evaluate the accuracy, precision, and suitability of a wide variety of ocean color chlorophyll algorithms for use by the Sea Viewing Wide Field-of-view Sensor (SeaWiFS) (O'Reilly et al. 1998). This provided a method of analyzing SeaWiFS data effectively to be able to process it so that it can be used for the further development of processing algorithms. The dynamics and the optical properties of the turbid waters of the Hudson River outflow plume have been studied (Eppley et al. 1985, Johnson, Miller & Schofield 2003, Malone 1976). However, the classification of plumes by the relative contributions of chlorophyll, color dissolved organic matter (CDOM) and detritus was not achieved (Johnson, Miller & Schofield 2003).

The absorption and scattering properties of a medium for light of any given wavelength can be measured in terms of the absorption coefficient, the scattering coefficient and the volume scattering function. These are referred to as inherent optical properties (IOPs). One way of understanding the response of different regions to changes in the IOPs is by classifying water masses. The earliest classification was done in (Jerlov 1951) to classify waters as Case I, II and III. These water types are used in data analyses

even today. Since then many attempts have been made to classify water types based on ocean optics. Such an approach using bioinformatic algorithms to classify water masses was presented in (Oliver et al. 2004). A functional gene expression classification algorithm using K-Means Clustering (MacQueen 1967) was employed to obtain water mass classification based on ocean color.

Chlorophyll retrieval has been traditionally done using band-ratios (Aiken et al. 1995, Austin, Petzold 1981, Carder et al. 1999, Clark, Baker & Strong 1980, Gordon et al. 1983, Lee, Carder 2000, Morel, Prieur 1977, O'Reilly et al. 1998) and spectral curvature (Barnard, Zaneveld, J. Ronald V. & Pegau 1999, Campbell, Esaias 1983). Other studies (Roesler, Perry & Carder 1989, Roesler, Perry 1995) an inversion technique to estimate absorption, emission and backscattering spectra was used, which laid the basis for using water-leaving radiances for determining the components of the reflectance spectrum. However, band-ratio algorithms are known to remain sensitive over a wider dynamic range of absorption values and perform better at low- and high-absorption values than spectral curvature algorithms (Lee et al. 1998). Hence, band ratio was the technique chosen for the work carried out in this thesis.

In terms of picking out similar ecosystems around the world, only a few comparisons have been made. In (Mueter et al. 2007) a comparison based on physical responses of 4 Large Marine Ecosystems was made, but it was limited to the Bering Sea and the Gulf of Alaska in the Pacific Ocean. In (Iwasaki, Kubota & Tomita 2006) a comparison of two global SST datasets comparing Center for Atmospheric and Oceanic Studies (CAOS) and Reynolds SST (Reynolds 1988) data was illustrated. Also, SST data was evaluated along with buoy data to estimate the global ocean’s Turbulent Heat Flux

(THF). In (Barnston, Smith 1996) a method for the specification and prediction of global precipitation using global SST datasets using Canonical Correlation Analysis (CCA) was presented.

In (Harada et al. 2006) it was shown that the alkenone SST reconstruction for the Okhotsk Sea is directly linked to the effects of climate change in the Sea of Japan and thereby reflects global climate change, but no satellite analysis was done. In (Reynolds 1988) an analysis of real time in situ and satellite SST data was done for the two-year period of January 1985 to December 1986 which showed the combined advantage of both these data. In (Reynolds, Smith 1995) an analysis of global SST climatology over a period of 12 years from 1985-1993 using in situ, satellite data and sea-ice cover was made. In (Kaplan et al. 1998) the author analyzed global SST data from 1856-1991 using statistical analysis methods to predict physical oceanographic phenomena such as El Niño – Southern Oscillation. Although these analyses were done on global data, they were mainly used to identify spatially small scale variations in SST. A large scale global analysis was not done and hence this was chosen as the basis for the correlation between similar coastal regions of the world.

All of this work has significantly advanced our understanding of the behavior of large marine ecosystems all over the world by quantifying the relationship between their physical and biological behavior. The hypothesis that the coastal regions off of North America and Asia behave similarly has been expounded for the first time in this thesis and using SST data as a basis for validating this hypothesis is also a first. Towards this end, analyzing global SST data to obtain seasonal variability has been done for the years 1995-2005 and even though this is a relatively short time period to identify any large

patterns pertaining to climate change, interesting results have been obtained in terms of the bigger objective of identifying similar estuarine coastal systems as well as identifying ocean-atmosphere phenomena such as El Niño. Applying band ratios to identify water masses in the eastern coast of Asia has been tested for the first time here as well.

Datasets Used

SeaWiFS:

The Sea viewing Wide Field-of-view Sensor (SeaWiFS), is the scientific payload aboard the Sea Star spacecraft. This satellite, which began as an extension to the Coastal Zone Color Scanner (Hovis et al. 1980) provides useful information about the bio-optical properties of the global ocean. The SeaWiFS sensor operates in 8 bands ranging from 402 to 885 nm wavelengths (Table 1). The satellite broadcasts SeaWiFS data in real time to the Goddard Space Flight Center (GSFC) High-Resolution Picture Transmission (HRPT) station, as well as to other stations, and data are recorded as Global Area Coverage (GAC) and Local Area Coverage (LAC) by the National Aeronautics and Space Administration (NASA) GSFC. These HRPT, GAC, and LAC data are then transferred to the SeaWiFS Data Processing System (SDPS). The data processing element receives raw spacecraft data and generates standard global ocean color data products. The standard products go to the GSFC Earth Observing System Data and Information System (EOSDIS) Distributed Active Archive Center (DAAC) which is responsible for archiving and distributing SeaWiFS data (Feldman 2008).

SeaWiFS data goes through 3 stages of processing, starting at Level 0 and going to Level 3. Level 0 data contains the raw radiance counts from all bands and spacecraft and instrument telemetry information. SeaWiFS Level 0 data is processed to Level 1 by appending calibration data, navigation data, instrument telemetry information, and selected spacecraft telemetry information to form a Level 1 Hierarchical Data Format (HDF) file that contains raw radiance values for each of the eight SeaWiFS bands. The HDF file is a library and multi-object file format for the transfer of graphical and

numerical data. HDF is the prescribed format for standard data products that are derived from Earth Observing Systems (EOS) missions (The HDF Group 2008).

A Level-2 data product is generated from a Level 1 product. The main data contents of the product are the geophysical values for each pixel, derived from the Level 1 radiance by applying sensor calibration, atmospheric corrections, and bio-optical algorithms. Each Level-2 product corresponds exactly in geographical coverage (scan-line and pixel extent) to that of its parent Level 1 product and is stored in one physical HDF file.

The form of a Level 2 file name is Syyyydddhhmmss.L2_ccc, where S – SeaWiFS; yyyydddhhmmss are the GMT year, Julian day of the year, hours, minutes, and seconds of the first scan line; and ccc is the coverage: MLAC for merged LAC (multiple scenes from a single orbit merged into a single product).

As mentioned before, the SeaWiFS data have 3 product data types - GAC, LAC and Merged LAC (MLAC). LAC refers to all full-resolution, recorded data. GAC data are sub-sampled from full-resolution data with every fourth pixel of a scan line from LAC and every fourth scan line being recorded. Merged LAC (MLAC) consolidates all available full-resolution data (LAC and HRPT) from a single orbit (Feldman 2008). This thesis has used Level 2 MLAC data because of the real-time availability and full resolution.

The specific attributes of the data used in this thesis are (Feldman 2008):

- Data Time
    - Start Time (character): start GMT of the first scan line of the scene; concatenated digits for year, day-of-year, hours, minutes, seconds, and fraction of seconds in the format of YYYYDDDHHMMSSFFF.
    - End Time (character): start GMT of the last scan line of the scene; concatenated digits for year, day-of-year, hours, minutes, seconds, and fraction of seconds in the format of YYYYDDDHHMMSSFFF.
- Scene Coordinates
    - Latitude Units (character): "degrees North"; units used for all latitude values in this product.
    - Longitude Units (character): "degrees East"; units used for all longitude values in this product.
    - Upper Left Latitude (4-byte real): latitude of the upper left scene corner.
    - Upper Left Longitude (4-byte real): longitude of the upper left scene corner.
    - Upper Right Latitude (4-byte real): latitude of the upper right scene corner.
    - Upper Right Longitude (4-byte real): longitude of the upper right scene corner.
    - Lower Left Latitude (4-byte real): latitude of the lower left scene corner.

- Lower Left Longitude (4-byte real): longitude of the lower left scene corner.
- Lower Right Latitude (4-byte real): latitude of the lower right scene corner.
- Lower Right Longitude (4-byte real): longitude of the lower right scene corner.

- Geophysical Data: The following data objects are science data sets belonging to the Geophysical Data Vgroup (Table 2).
  - nLw_WWW (2-byte integer, array size Number of Scan Lines x Pixels per Scan Line), where WWW is the band wavelength: long_name = "Normalized water-leaving radiance at WWW nm"; units = "mW cm^{-2} um^{-1} sr^{-1}"
  - chlor_a (4-byte real, array size Number of Scan Lines x Pixels per Scan Line): long_name = "Chlorophyll Concentration, OC4 Algorithm"; slope = 1.0; intercept = 0.0; units = "mg $^{m-3}$

Level 3 processing involves both temporal and spatial binning (discretizing the location values into a small number of groups associated with geographical areas (Oracle Inc 2005) and utilizes Level 2 GAC data as input. The Level 2 GAC data is sub sampled by a factor of two to produce the Level 3 product (Feldman 2008).

Two sets of SeaWiFS data were used in this thesis. The first, for the NJ shelf was obtained from the IMCS in-house satellite data archive. The second set was downloaded from the NASA SeaWiFS web Graphical User Interface (GUI) available upon request from the Ocean Color Website. The data used for the NJ shelf were daily data; however, the data used for the Asian coast were 8-day composited data. The reason for this was

that daily data available during that time period was extremely cloudy and very few data points were available for applying the water mass algorithm to. Hence, in order to obtain sufficient samples, 8-day composites were used. As seen in the Results section, these data were still very cloudy and there were many patches of no data, which is but a slight improvement on the daily data.

AVHRR:

The Advanced Very High Resolution Radiometer (AVHRR) is a 6 channel radiation-detection imager that can be used for remotely determining cloud cover and the surface temperature. The term "surface" can mean the surface of the Earth, the upper surfaces of clouds, or the surface of a body of water (NOAA 2008). This scanning radiometer uses 6 detectors that collect different bands of radiation wavelengths (Table 3).

The SST data used to obtain the yearly summer/winter differences were obtained from the NASA website PO.DAAC, short for the Physical Oceanography Distributed Active Archive Center at the Jet Propulsion Laboratory/Caltech, which distributes SST data at various spatial and temporal resolutions. The Pathfinder AVHRR SST product is a dataset derived from the NOAA polar-orbiting series of satellites that start with NOAA-9 in 1985. This dataset represents a reprocessing of the entire AVHRR time series using better SST algorithms (McClain, Pichel & Walton 1985), improved satellite calibration, quality control and cloud detection (Stowe et al. 1991). These data can be downloaded from the website either via FTP or by using the PODAAC Ocean Earth Science Information Partner (ESIP) Tool (POET) GUI that allows for spatial and temporal subsetting.

The AVHRR sensor provides for global collection of data from all spectral channels. Each pass of the satellite provides a 2399 km (1491 mi) wide swath. The satellite orbits the Earth 14 times each day from 833 km (517 mi) above its surface.

The NOAA AVHRR processing flow begins with sensor data receipt by the Command and Data Acquisition (CDA) stations where the data are re-broadcast via communications satellites, to NOAA/National Environmental Satellite, Data and Information Services, where the data are processed, archived, and reproduced (USGS 2006).

The dataset has a spatial resolution of 4 km with an equal area-equal angle projection (Kidder, Vonder Haar 1995). The data are binned in an equal area grid of resolution approximately 4.64 km, making the data array size (8192x4096). The daily data are stored in the Scientific Data Set HDF-SDS (Vazquez 2004). The advantage of this dataset is that it is not nested at all, and the data array is very easy to extract from the main data structure.

The processing is done in the following way. Level-1B data are first ingested from optical disk, then converted from to a standard image format. Data are then navigated from line/pixel (image) coordinates to latitude/ longitude coordinates and subsetted. Next the non-linear correction algorithm adjusts for the calibrations of the AVHRR channels, and SST is computed from predetermined regression coefficients, which are specific to 3 regimes of atmospheric water vapor (Brown, Brown & Evans 1993).

Once SST retrievals are determined, the data subsets are binned to produce the 9.28 km equal-area orbitals for both ascending and descending nodes, and an initial quality flag is assigned to each retrieval. After the orbitals for an entire day have been completely processed, they are composited to a single daily file (McClain, Pichel & Walton 1985).

The next phase is declouding. This is achieved through the creation of composite images over 3 weeks, from each of which a mean is computed. These are then used to fill a central weekly mean image which contains the day being declouded (if the central mean image is missing values). If the weekly means from week (n- 1) or week (n+1) cannot be used to fill empty values in the central (week n) mean, a spatial interpolation is done. The completely-filled weekly image is then compared to the central daily, and simple thresholding was used to indicate partial or complete cloudiness. This process generates a cloud mask for every day of data (Stowe et al. 1991).

All the SST data used in this thesis were downloaded from the Java-enabled web GUI from NASA's PODAAC website.

The data (both chlorophyll and SST) were downloaded as HDF files. They were processed and plotted in MATLAB.

LaTTE Shipboard Data:

The shipboard data used for the validation plots were taken from the surface CTD data aboard the R/V Oceanus, a ship used to perform field experiments during the LaTTE field effort. These data were the instantaneous salinity value at the location at which the CTD sensor was inserted. It represents the path that the ship took, which was, essentially to follow the path that the injected tracer dye was taking owing to the mixing processes that are responsible for the shelf transport in the Hudson River estuary.

These data are in the form of MATLAB files (*.mat) which can directly be read and processed in MATLAB.

Methods and Procedures

Water Mass Classification

This section describes the details of the classification algorithm developed and the procedures we use to develop this algorithm. The algorithm was conceived as an extension of the project started in (Bosch et al. 2004). Even though the main objective of that project was to prepare a chlorophyll budget for the Lagrangian Transport and Transformation Experiment (LaTTE) (Schofield et al. 2004b) domain of the Mid-Atlantic Bight (Fig. 5), the band ratio technique has since proved to be very useful in implementing the water mass classification algorithm as well. The LaTTE region is a subset of the MAB, covering the coastal shore of New Jersey, at the mouth of the Hudson River where it meets the sea. The experiment was started as an effort to study the mixing processes that influence the biological production rates by using dye tracers to track the paths that the water takes.

We deal with data for April 2005 because of the presence of the spring bloom and the beginning of the summer upwelling time (Glenn et al. 1996). This is SeaWiFS ocean color data, downloaded from the NASA Ocean Color website housed in IMCS' computers.

The main idea is to learn the specific contributions of the component quantities to the ocean productivity as remotely sensed by satellites, as described in the Ocean Optics section. Consequently, the nLw_490, which corresponds to the CDOM proportion and the nLw_670, which corresponds to the phytoplankton spectra, are the two quantities whose bands are ratio-ed. nLw_490 is in the numerator and nLw_670 is in the denominator for this band ratio.

Once the ratios are obtained, thresholds are set on the resulting array. We make 0-1.9 one water mass, 1.9-3.3 a second and 3.3-5 is set as the third class. We aim to obtain 3 water classes, viz. freshwater at the mouth of the Hudson River, water that has been transported across the shelf and has relatively less nutrients and hence less chlorophyll content (indicating less primary production) - which we will assign as aged water - and open ocean water, that has the least nutrients and consequently, least chlor_a.

The low values of the band ratio are used to indicate freshwater. The reason behind this is that in the ratio of (nLw_490: nLw_670), nLw_670 represents phytoplankton contribution. So, if phytoplankton contribution is high, then it must mean that the ratio has to be less because nLw_670 is in the denominator. This means smaller ratio values indicate higher phytoplankton, which in turn is indicated by higher chlorophyll values, which is in turn found in freshwater at the mouth of the river, because of higher nutrient input.

Following from this reasoning, intermediate values indicate water that has been transported across the shelf, which is relatively depleted of nutrients and hence has less chlorophyll content.

The highest ratio values are used to indicate open ocean because these waters are usually less productive and hence have a moderate amount CDOM. Hence, if the ratio value is high, then it means the contribution due to CDOM is high, which is indicated by the nLw_490 value. CDOM is independent of phytoplankton biomass and hence is found in oligotrophic waters as well.

Once this is done, the ratio-ed data array is plotted using MATLAB in a pseudo-color plot. The three water masses are assigned three colors in order to visually indicate

the differences in the regions. A land mask is applied to mask out the land and bathymetry data is added using previously created master files which are also native to the IMCS in-house satellite data archive. Since the data is already stored in gridded format, the latitude longitude grids do not have to be created. This is one step away from the final output.

The last step is to validate the classification algorithm. This is done by making use of the ship-board data from the field experiments conducted during the LaTTE experiment for the same time as that of the satellite data, i.e. April 2005. The salinity data from that time are overlaid on the surface ocean color data. This data are in the form of tracks that the ship followed during the experiment. The objective of this step is to show that the regions or boundaries of changing salinity values represent the boundaries between different water types. The plotted salinity track is assigned a different color scale for clarity and aesthetic improvement. The success of the developed technique depends on how well the water masses match the salinity changes.

As an added validation step, the threshold values are changed by $\pm$ 25% to check whether the assumed thresholds are correct and the salinity tracks are again overlaid. This is done for two random images and not all of them. As expected, the salinity tracks do not match with the classified water masses.

Sea Surface Temperature:

This section describes the methods used to analyze global sea surface temperature data. The data is obtained from NASA's PODAAC web GUI as mentioned

in the Datasets section. Since it is a global dataset, the array sizes are very large (4074x8171) and need to be processed on a powerful machine with a large memory.

The initial hypothesis is that regions with similar latitude locations around the world will exhibit similar behavior so that the water mass classification technique can be applied to such regions. Also, the MAB is influenced by the Gulf Stream and the East Asian coast is influenced by the Kuroshio Current. This provides a basis for our hypothesis. In order to prove this, SST analyses are made using basic statistical techniques and conclusions are drawn.

We use SST AVHRR data for the months of August and February (depicting peak summer and winter months) for the years 1995-2005. This data has 8 quality flags (0-7), which are set according to whether each data pixel has passed a given set of tests (Kilpatrick, Podesta & Evans 2001). 0 is the lowest quality and 7 is the best. However, even though 7 is the best quality it means that the global map has fewer pixels that have passed all quality tests, and consequently fewer actual data pixels. Conversely, it follows that quality flag 0 will have more data pixels filled in, even though they may not all be reliable in terms of having passed the desired quality tests. Hence, to obtain a desirable cross between reliability and number of data pixels present, flag 2 was chosen because it had sufficient pixels to analyze and the reliability was also good enough to make global plots.

For each year, the absolute difference between the summer and winter temperature is calculated and the results are plotted. Next, 11-year warmest pixel and mean composites are made. Once the mean is obtained, each year's mean anomaly (the

difference between the mean and that year's temperature) is calculated and plotted. Also, RMS variability for the 11 years is calculated, in order to estimate the standard deviation of each pixel from the mean. Looking at the time series of the 11-year SST data, upwelling years are focused upon and the summer of the year 2002 is chosen as a good time to apply the water mass algorithm because the SST plots indicate upwelling in the Asian coast during August 2002. It is also seen from the seasonal variation plots that the Gulf Stream comes out as a cold anomaly. All of these operations are done using programs coded in MATLAB.

Global Application of the Developed Technique:

Once it has successfully been shown that due to the similarity in latitudinal range, the two regions of the MAB and the East Asian coast are similar, we test the applicability of the water mass tagging algorithm to another similar region by applying it to the East Asian coast.

The procedure is remarkably similar; we start by taking band-ratios of the two nLw's. Then a thresholding function is applied which classifies the water masses according to the range in which the ratio values lie. The only difference is that there are no shipboard salinity data available that can track the offshore transport in these waters. This means that the final validation step could not be carried out.

A look at the results tells us that the hypothesis that this technique could be standardized to apply to other global regions is correct. The algorithm successfully identifies river and open ocean bodies in the Asian coast in the Okhotsk and Yellow seas.

Although there is no field data to support the results produced by the application of the algorithm to these regions, an informed estimate can be made regarding where river input can be expected, from knowing the approximate locations of the river basin systems that flow into these seas. This offers bright prospects for future work that can be conducted in this direction and also motivates the necessity for field experiments to be undertaken in these regions.

Results and Discussion

As mentioned earlier, the water mass classification algorithm developed in this thesis is based on the band-ratios which represent the specific contributions of the individual components such as CDOM and phytoplankton absorption values. Once the data has been band ratio-ed and plotted we apply thresholds to classify the water into 3 different water masses – river plume water, transported water and open ocean water. Once the water classes are obtained, ship salinity tracks from shipboard data collected during the LaTTE field effort are overlaid on the classified results and validation is performed. Figs. 6 a-g show the final results with a gray scale colormap applied to the classified water masses and a rainbow colormap applied to the overlaid salinity tracks. It can be seen that at the boundary of each different water mass, the salinity value changes (as seen from the changing color of the track), which is an indicator of the correctness of the algorithm.

The algorithm is applied to SeaWiFS data for the month of April (10^{th} to 18^{th}) and salinity data used is also for the same days. It can be seen that the innermost (black) water mass corresponds to the freshwater coming in from the Hudson at the mouth of the estuary. The intermediate gray colored mass belongs to the water that has been transported offshore by hydrographic paths, the nutrient content is relatively less and hence the plume material is also less than that for freshwater, which indirectly means that the chlorophyll content and hence the phytoplankton biomass is relatively less. The third and last water type is the faint gray (almost white) shaded one, which represents the open ocean. These waters could be oligotrophic and hence the biomass is very less, which means the band ratio is highest in this region. The plume material is transported offshore

and is dissipated probably due to export flux and grazing. It is seen that the material converges approximately at the 40 - 60m isobath.

Plotting the ship salinity values vs channel ratios (Fig. 7c) shows us that the estuarine salinity is about 16-17 ppt. The intermediate water class displays a salinity of 19-26 ppt. Everything above 26 ppt. belongs to the open ocean water class. This is consistent with the chosen thresholds. Also, we changed the threshold values to $\pm$ 25% (Fig. 7a-b) and it is seen that the classification appears inconsistent with what are known river and open ocean bodies. So, changing the threshold values makes the classification incorrect. This shows that the empirically chosen threshold values have been validated.

Lastly, a plot of the satellite chlorophyll vs the measured in situ chlorophyll values (Fig. 7d) reveals the correlation between the satellite measurement and the actual chlorophyll values. This plot is roughly exponential with a positive power (a^{+b}) for lower values and more linear for higher values. This means that the satellite measured value is an underestimation of the actual chlorophyll values. However, it gets better at higher chlorophyll values, the values that really matter to the water mass classification algorithm because they are freshwater values.

Figs. 8 a-k show the 11 year time series of the global SST summer-winter differences. A close observation of each plot shows us that the hypothesis that the regions off the east coast of Asia is similar to the MAB because of similar latitude locations and the fact that both regions are influenced by warm western boundary currents. The plots also show that the seasonal differences are zero along the equator, which is as expected, because the tropical regions exhibit little or no seasonal variability. The temperate, mid-

latitudes are the regions that exhibit maximum seasonal variability and this is true of both the regions off North American and Asia. It is interesting to note, however, that the Gulf Stream comes off as a cold anomaly. One of the reasons for this might be that the winds blowing across the Atlantic near the Gulf Stream might have some moisture content in them, causing the temperature of the Gulf Stream to appear lower than usual.

These plots also point to the El Niño of 1997-1998 because the difference plot for the year 1998 is the only one that shows a finite difference value (other than zero) off the coast of Peru. It can also be seen that the El Niño year may have had an effect on the seasonal variation of the Mid-Atlantic Bight because the absolute difference values for that year were higher than for the other years (Fig. 8d), while the seasonal variation along the Asian coast remained more or less unchanged over the 11 year period (Fig. 11).

Figs. 9 a-b show the 11 year mean composite for the winter and summer respectively. The temperatures off the two regions of interest (ROIs) are remarkably identical, as seen from the mean plots. Fig. 9c shows the mean seasonal variability for the 11 years, which again supports the theory that the two regions have similar temperature behavior. The Gulf Stream appears cold here as well.

Similarly, we can make the same observations about Figs. 10 a-c which are warmest pixel composites for the same time period. It is interesting to note, however, that the Gulf Stream does not appear cold in these figures because the warmest pixel composite does not pick up the average (colder) temperatures. This is consistent with the hypothesis that Gulf Stream only appears as a cold anomaly in the seasonal and mean plots because of moisture-laden winds that reduce the apparent temperature.

Figs. 11 a-d show the mean summer and winter anomalies for the years of 1997 and 1998, which marked the advent of perhaps the greatest El Niño event in the last 50 years (McPhaden 1999). As can be seen clearly from the plots, the anomaly for the winter of 1997 was zero. During the summer of 1997, the El Niño began to set in and high temperature anomalies can be seen. This continued on through the winter and in the Feb image for 1998, we can see the ENSO very clearly. The summer of 1998 bears lesser signs of the ENSO phenomenon which was about the time when markings of the El Niño beginning to recede can be seen.

Figs. 12 a-b show the RMS variability of the 11 year time series. Expectedly, most regions show little or no variability and the two ROIs have similar standard deviations as well. This is the last of the SST plots used in this thesis.

Zooming in on the coasts of USA and China, during the year 2002 (Figs. 13 a-b), we can see at closer quarters the similarity in the temperature of the two regions. Since the summer months have upwelling, the summer-winter difference along both these regions is greater than zero. This year's SeaWiFS data is used to apply the water mass tagging algorithm to the Asian coast because clearer data was available for the August of 2002. Also, due to the monsoonal climatic conditions of this region, the summer time represents the maximum river input, which could be likened to the spring time in the MAB.

Figs. 14 a-e show the results of the water mass classification as applied to the Asian coastal region. As can be seen from the figures, the algorithm is successful in identifying river and open ocean water. The identified estuarine systems are those of the

Amur and the Penzhina in the Okhotsk Sea; and the Yangtze, and the Huang-Ho rivers in the Yellow Sea. It can be seen from these plots that a coastal current develops along the coast of China in the Yellow Sea and flows off-shore into the Pacific. A similar current builds along the coast of Russia in the Okhotsk Sea and flows northward. If we were to liken this region to the mouth of the Hudson River, this coastal current would be bounded by Long Island coast, but since such a land mass is not present in the Okhotsk Sea, this coastal current develops in other directions due to wind forcing.

The scales on which the identification was done for each region were different. The LaTTE domain is but within a range of 2° in latitude and longitude. But, the East Asian plots cover a spatial range of over 50° in latitude and longitude. This was because of the lack of clear data zoomed-in to such a minute scale because on such scales the East Asian coast is extremely cloudy. Another issue was that of lack of field data available to validate the classification algorithm applied to the Asian coast. However, a look at the maps of the river systems of these regions tells us that water masses have been identified in the regions where river plumes are expected to be found and so, this offers us a somewhat rough validation of the technique developed.

Open Research Issues

One further step could be to apply the algorithm to the smallest scales as suggested previously, to include a spatial grid of only a few degrees vertically and horizontally. The LaTTE region was one such region with a few degrees of latitude and longitude being covered. However, the coastal region of Asia is of a bigger spatial grid because of the clouds present in the nearshore coastal region of Asia, which makes it difficult to apply the classification technique to this region. Also, the technique could be applied to other Large Marine Ecosystems as a tool to estimate the approximate productivity in a region. It would be useful to identify similar coastal regions using parameters other than latitudinal or temperature similarities alone. It would also be helpful to study and understand the wind forcing in the Asian coast to make better comparisons between these regions and the coast of North America.

The SST plots can be used to identify long-term changes in the oceans, such as global climate change. Although the time frame used in this thesis is too small to identify any significant climate differences, it can be considered as a step in the direction. These plots also serve the purpose of identifying upwelling along the coastal regions of Peru, which was identified as ENSO in the results section earlier.

The cold Gulf Stream anomaly may be an example of the requirement of better cloud detection algorithms in order to perform accurate analyses.

Identifying regions in the ocean that are warm or cold using the SST plots can be done to improve fisheries management policies, by identifying and focusing upon regions that might be conducive to industrial and commercial fishing. Combined with the water

mass tagging technique to identify nutrient rich waters, this can prove to be quite an innovative tool for fisheries' managers.

Summary and Conclusions

The water mass tagging algorithm is an innovative technique that uses band ratios to identify water masses based on their component concentrations. Thus, we can say that band ratios are an effective way to classify water masses. It is a highly effective tool for identifying rivers and non-river waters especially in regions such as the MAB, which is characterized by high productivity.

Regions of similar behavior were identified along the coastal regions of North America and Asia, using global SST analysis. The SST plots have proven very useful in identifying temperature variations on a global spatial scale. They also help in understanding global seasonal temperature variations as well as in identifying coastal upwelling processes. Using these plots to predict large scale processes such as climate change, small scale seasonal variations or even ENSO-like phenomena would be a good idea.

The developed water mass technique was successfully applied to a coastal region that was identified as being similar to the MAB, using the SST analysis. The technique worked effectively in the test region and identified river and non river water masses as well. It also identifies coastal currents in this region similar to the one in the MAB.

Satellite analyses by themselves have several advantages as do field measurements, but using the two techniques in conjunction has helped the research in this thesis tremendously. Such efforts as performed in this thesis only prove the enhanced usefulness of remote sensing techniques in oceanography. This demonstrated the

usefulness of satellite imagery to (a) Define water masses locally; (b) Find similar areas globally; (c) Apply the algorithms in remote locations.

Tables

Band	Wavelength	Primary Use
1	402 – 422 nm	Dissolved organic matter (incl. Gelbstoffe)
2	433-453 nm	Chlorophyll absorption
3	480-500 nm	Pigment absorption
4	500-520 nm	Chlorophyll absorption
5	545-565 nm	Pigments, optical properties, sediments
6	660-680 nm	Atmospheric correction and sediments
7	745-785 nm	Atmospheric correction, aerosol radiance
8	845-885 nm	Atmospheric correction, aerosol radiance

Table 1: A listing of the bandwidths and primary uses for SeaWiFS (Feldman 2008)

Parameter	Storage (bytes)	Approximate Range	Units
nLw_WWW	2	0 - 32	mw cm^{-2} um^{-1} sr^{-1}
chlor_a	4	0 - 100	mg m^{-3}
K_490	2	0 – 6.4	m^{-1}
tau_WWW	2	0 – 3.2	none
angstrom_WWW	2	-6.4 – 6.4	none
eps_78	1	0 – 2.5	none

Table 2: Summary of Level-2 geophysical parameters (Feldman 2008)

Channel Number	Resolution at Nadir	Wavelength (μm)	Typical Use
1	1.09 km	0.58 – 0.68	Daytime cloud and surface mapping
2	1.09 km	0.725 – 1.00	Land-water boundaries
3A	1.09 km	1.58 – 1.64	Snow and ice detection
3B	1.09 km	3.55 – 3.93	Night cloud mapping, sea surface temperature
4	1.09 km	10.30 – 11.30	Night cloud mapping, sea surface temperature
5	1.09 km	11.50 – 12.50	Sea surface temperature

Table 3: AVHRR/3 Channel Characteristics (NOAA 2008)

Quality Flag	GAC Initial Tests	Reference Test	Suspect/Cloud Test	Uniformity Test	Zenith Angle Test
0	Fail/Pass	Fail	Fail	Fail	Fail
1	Pass	Fail	Fail	Fail	Pass
2	Pass	Fail	Fail	Pass	Fail
3	Pass	Fail	Fail	Pass	Pass
4	Pass	Pass	Pass	Fail	Fail
5	Pass	Pass	Pass	Fail	Pass
6	Pass	Pass	Pass	Pass	Fail
7	Pass	Pass	Pass	Pass	Pass

Table 4: Quality level tests for AVHRR data (Kilpatrick, Podesta & Evans 2001)

Figures

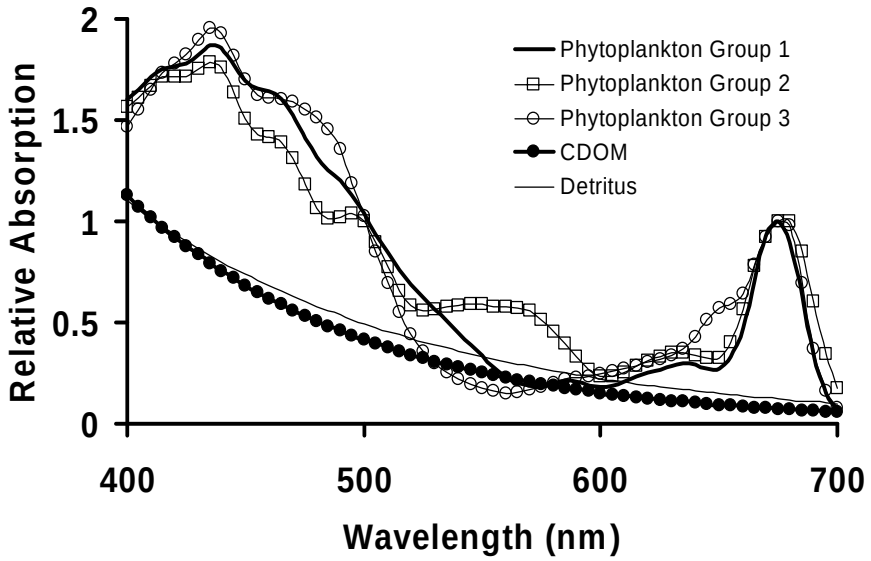

Fig. 1: Absorption spectra for constituent components (Kirk 1994)

Fig. 2: The Sea of Okhotsk (Alekseev et al. 2006)

Fig. 3a: The Japan Sea (NOAA 2003)

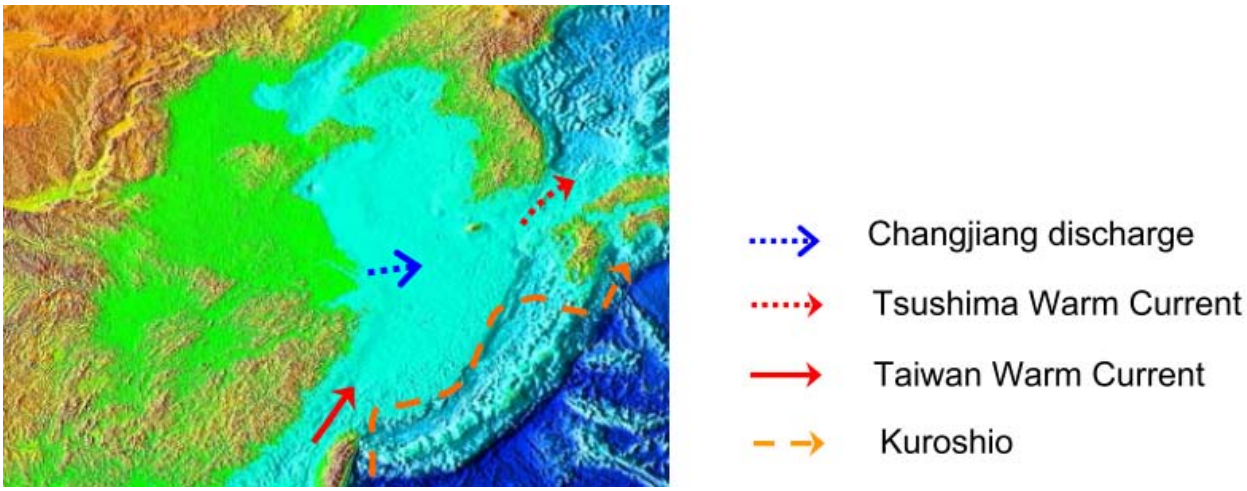

Fig.3b: Supply of freshwater to the Japan Sea (Terazaki 1999)

Fig. 4: Yellow Sea (Teng et al. 2005)

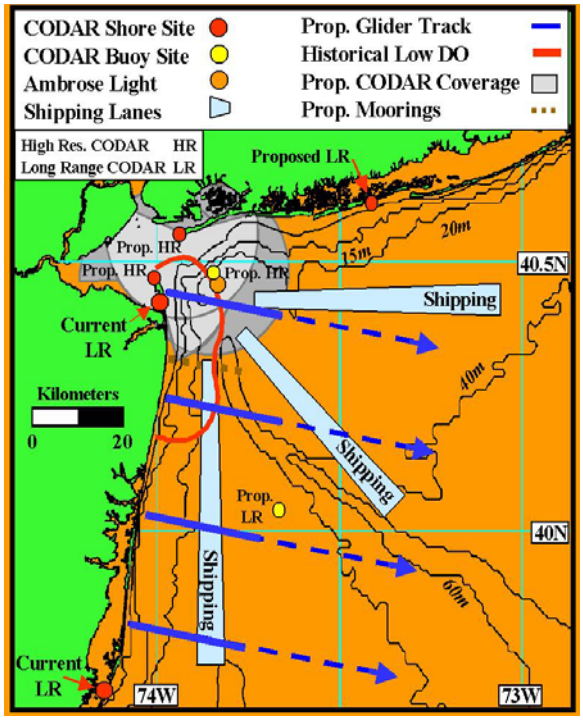

Fig. 5: The LaTTE Domain

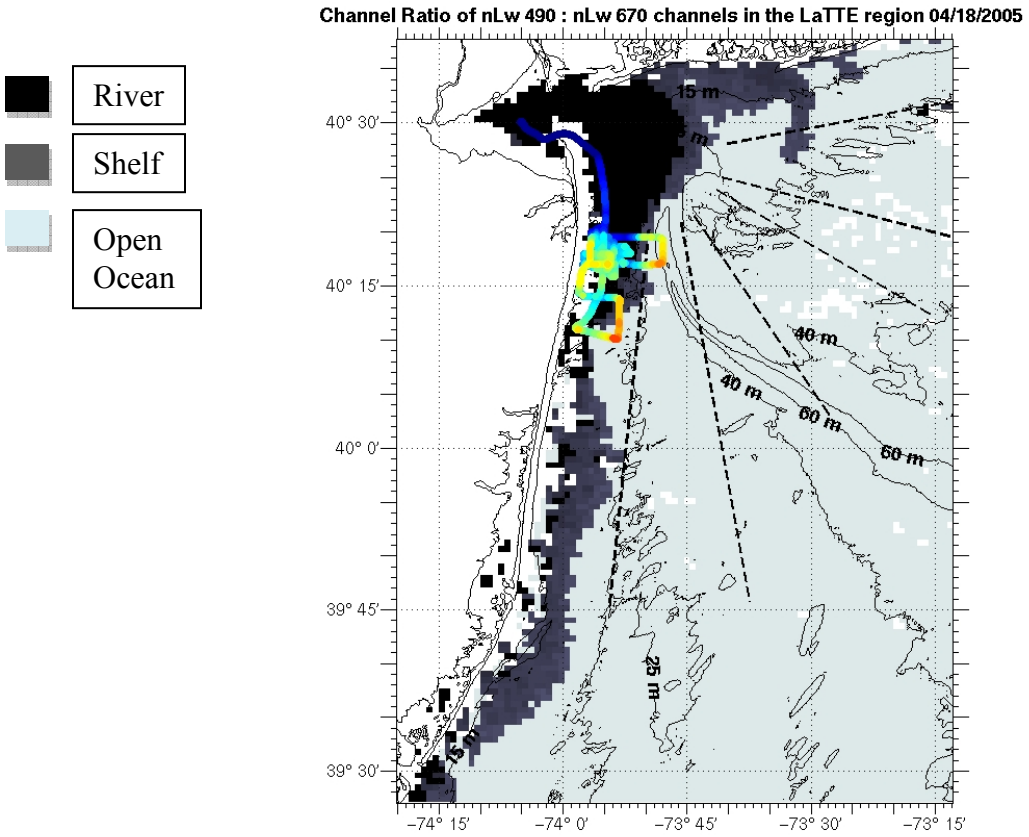
River
Shelf
Open Ocean
Channel Ratio of nLw 490 : nLw 670 channels in the LaTTE region 04/18/2005
40° 30'
40° 15'
40° 0'
39° 45'
39° 30'
-74° 15'
-74° 0'
-73° 45'
-73° 30'
-73° 15'
15 m
40 m
40 m
60 m
60 m
25 m
5 m

Fig. 6a.

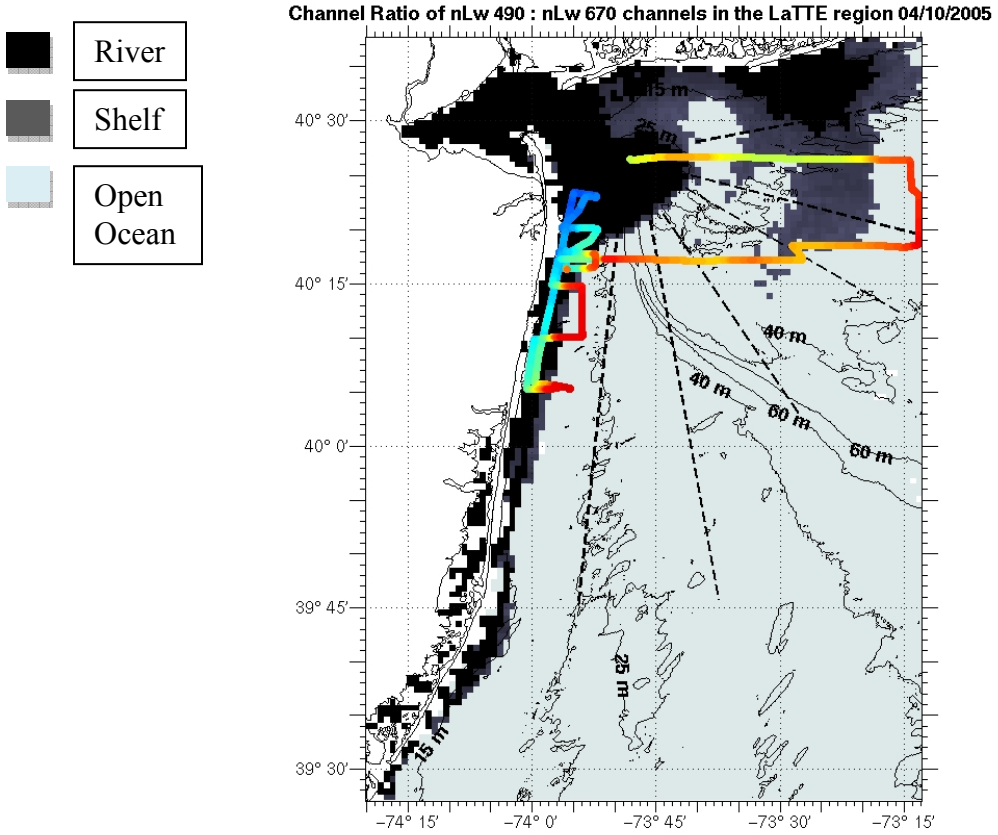
River
Shelf
Open Ocean
Channel Ratio of nLw 490 : nLw 670 channels in the LaTTE region 04/10/2005
40° 30′
40° 15′
40° 0′
39° 45′
39° 30′
−74° 15′
−74° 0′
−73° 45′
−73° 30′
−73° 15′
15 m
25 m
40 m
60 m

Fig. 6b.

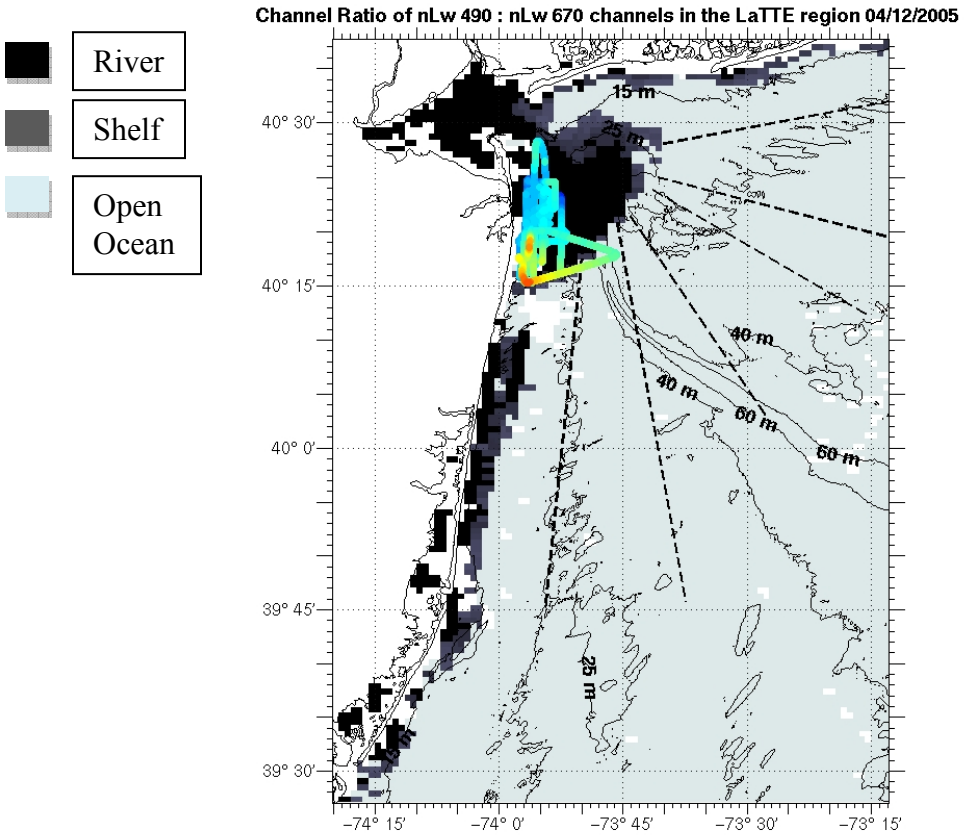
River
Shelf
Open Ocean
Channel Ratio of nLw 490 : nLw 670 channels in the LaTTE region 04/12/2005
15 m
25 m
40 m
40 m
60 m
60 m
25 m
40° 30′
40° 15′
40° 0′
39° 45′
39° 30′
−74° 15′
−74° 0′
−73° 45′
−73° 30′
−73° 15′

Fig. 6c.

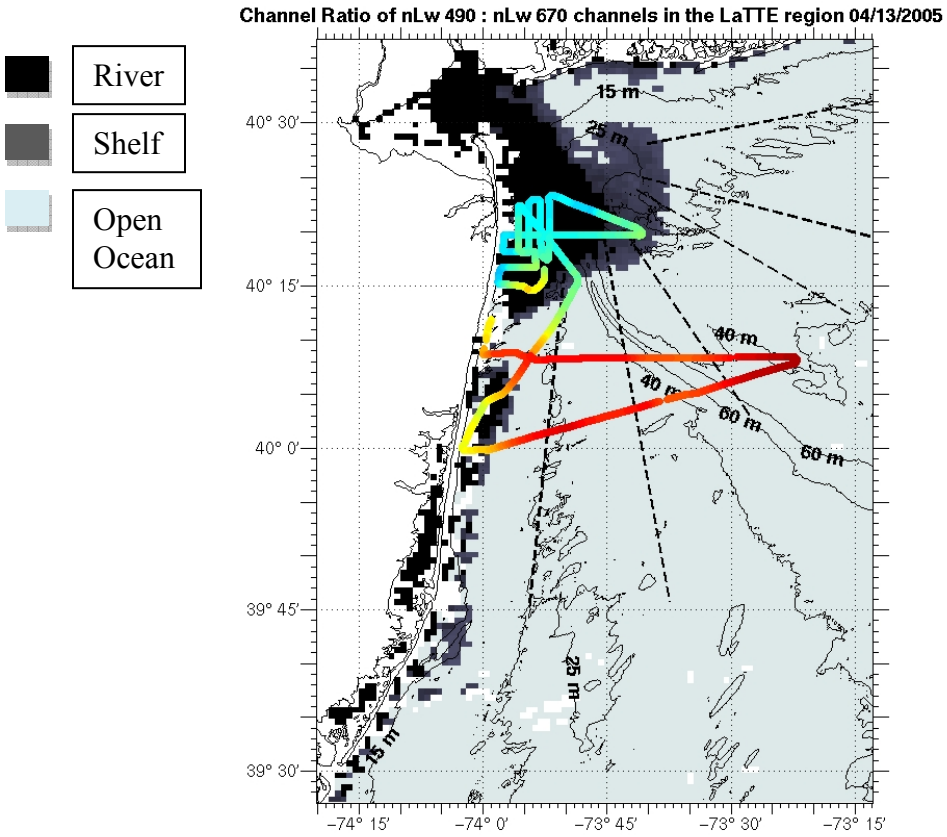
River
Shelf
Open Ocean
Channel Ratio of nLw 490 : nLw 670 channels in the LaTTE region 04/13/2005
15 m
25 m
40 m
40 m
60 m
60 m
25 m
15 m
40° 30′
40° 15′
40° 0′
39° 45′
39° 30′
−74° 15′
−74° 0′
−73° 45′
−73° 30′
−73° 15′

Fig. 6d.

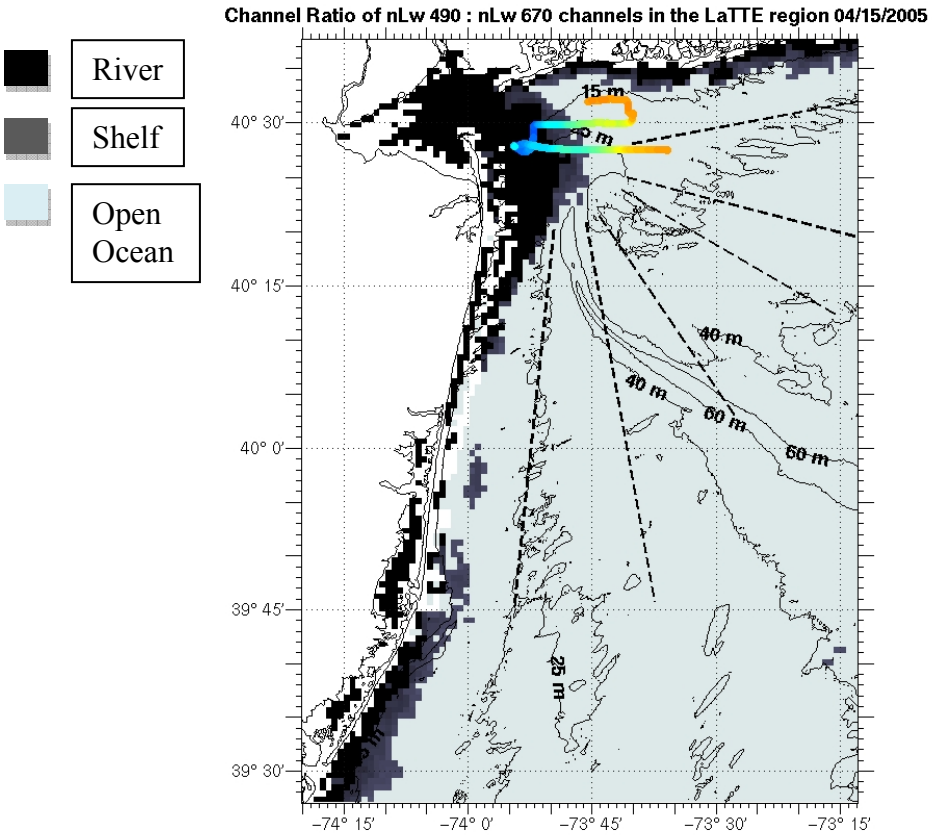
River
Shelf
Open Ocean
Channel Ratio of nLw 490 : nLw 670 channels in the LaTTE region 04/15/2005
15 m
40 m
40 m
60 m
60 m
25 m
40° 30′
40° 15′
40° 0′
39° 45′
39° 30′
−74° 15′
−74° 0′
−73° 45′
−73° 30′
−73° 15′

Fig. 6e.

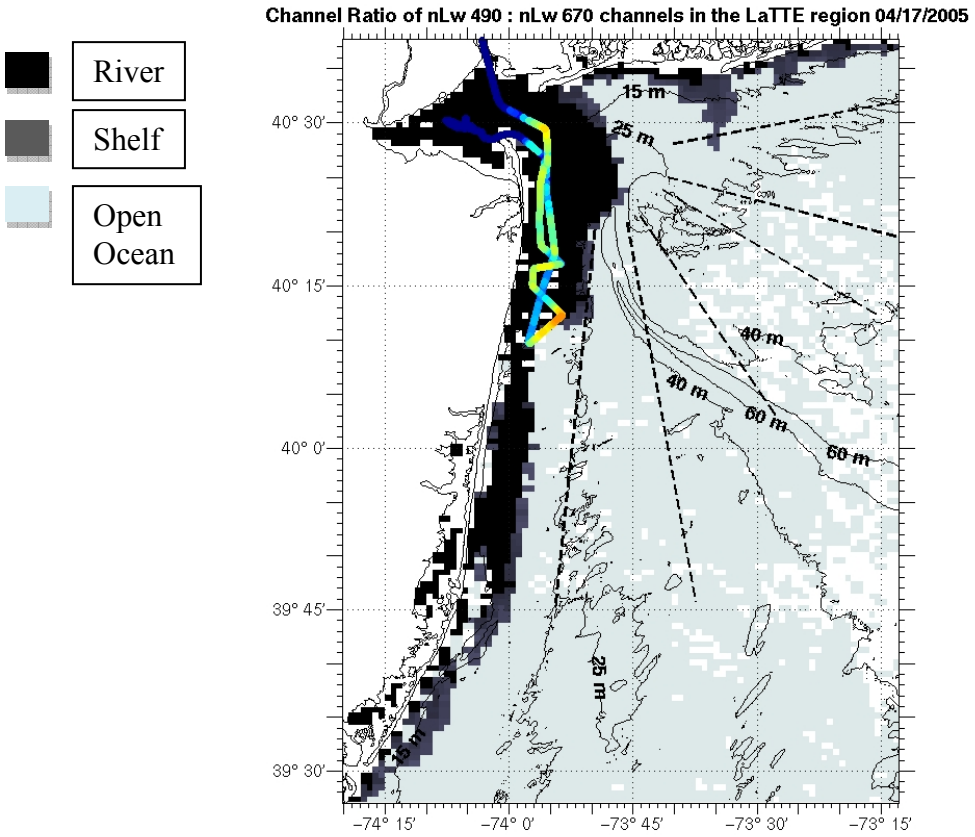
River
Shelf
Open Ocean
Channel Ratio of nLw 490 : nLw 670 channels in the LaTTE region 04/17/2005
15 m
25 m
40 m
40 m
60 m
60 m
25 m
15 m
40° 30′
40° 15′
40° 0′
39° 45′
39° 30′
−74° 15′
−74° 0′
−73° 45′
−73° 30′
−73° 15′

Fig. 6f.

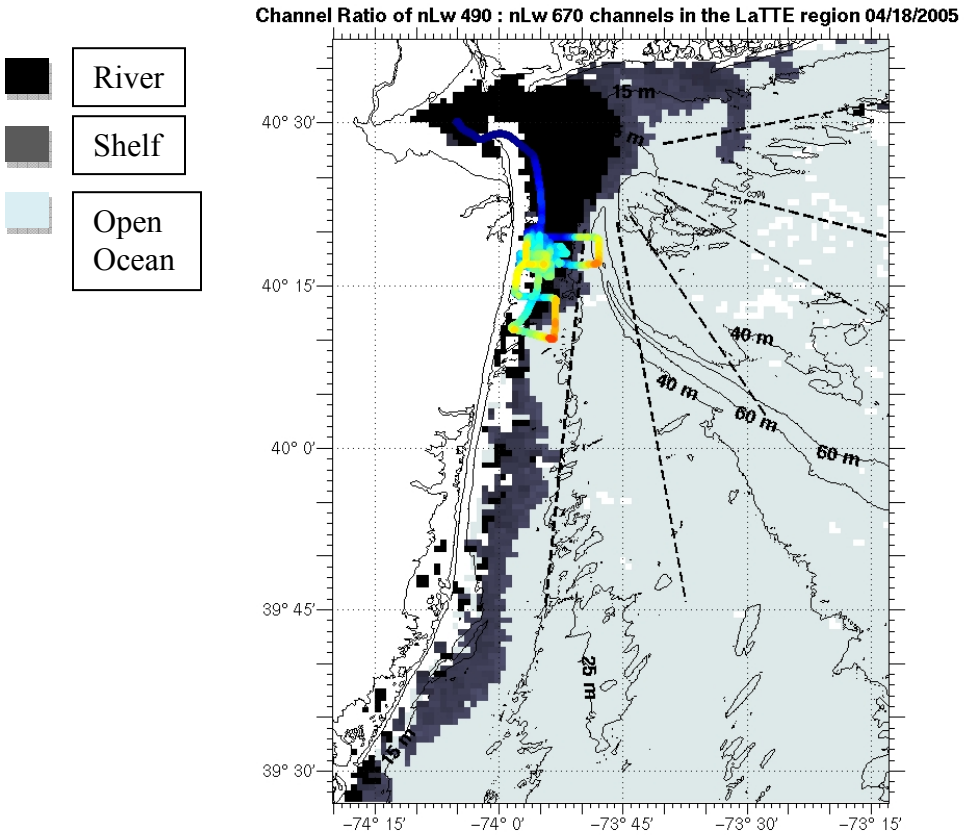

Fig. 6g.

Fig. 6: Results of the water mass classification algorithm in the LaTTE region with ship salinity tracks overlaid.

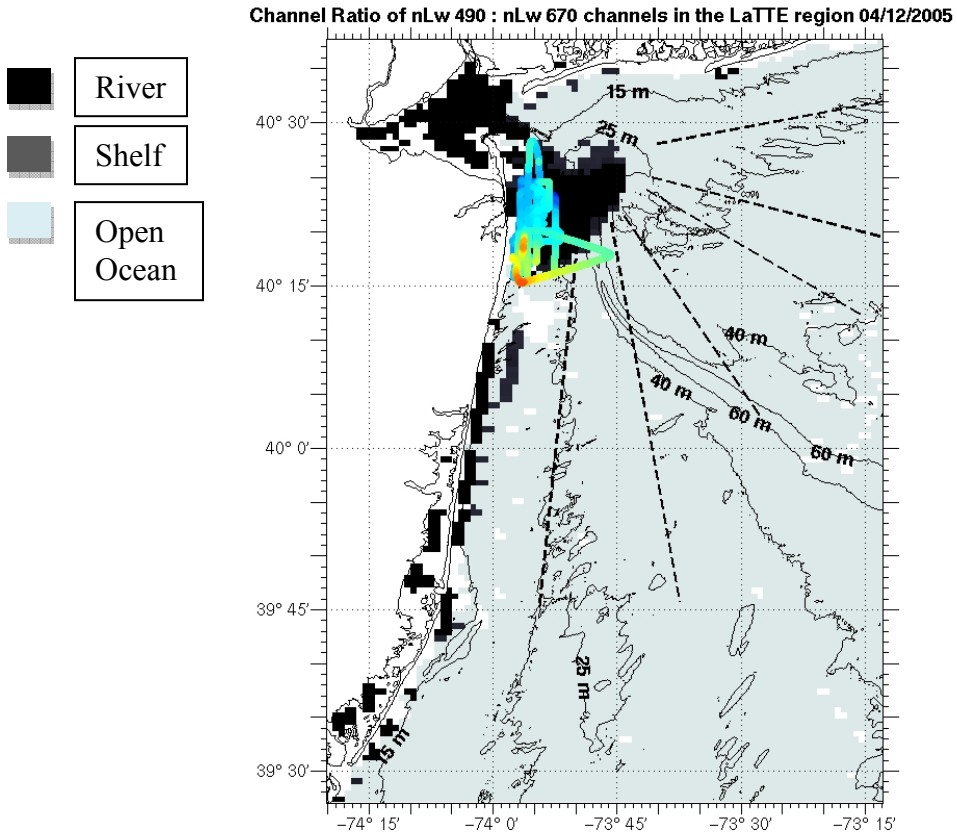
River
Shelf
Open Ocean
Channel Ratio of nLw 490 : nLw 670 channels in the LaTTE region 04/12/2005
15 m
25 m
40 m
40 m
60 m
60 m
25 m
15 m
40° 30′
40° 15′
40° 0′
39° 45′
39° 30′
−74° 15′
−74° 0′
−73° 45′
−73° 30′
−73° 15′

Fig. 7a.

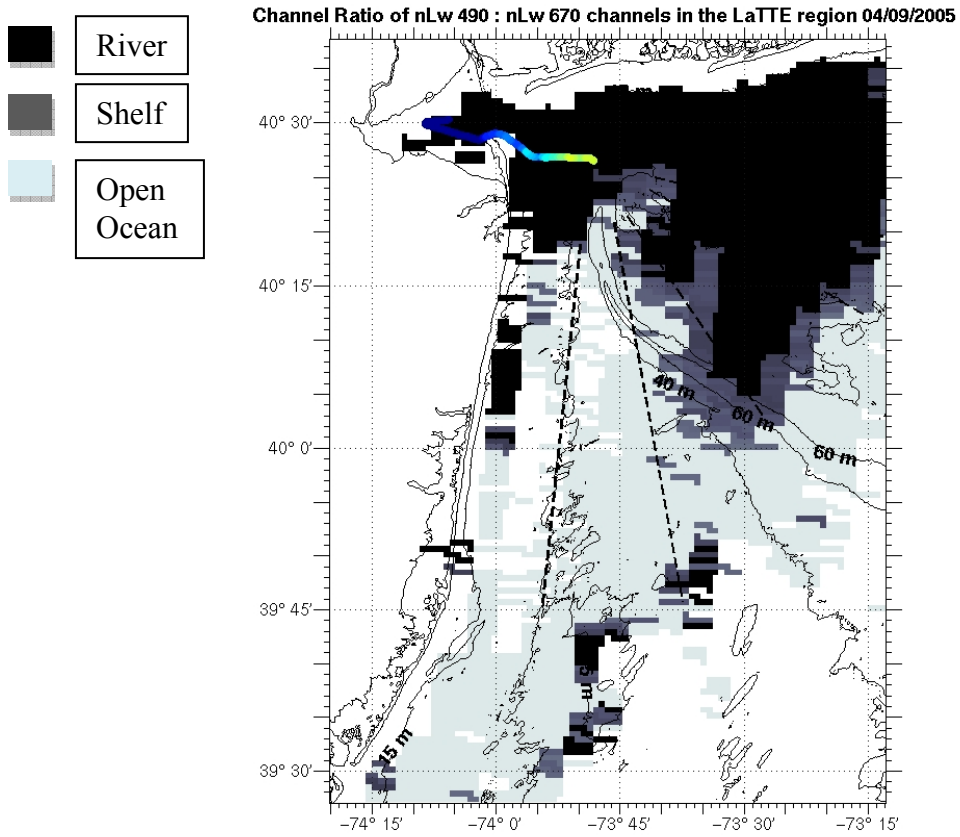
River
Shelf
Open Ocean
Channel Ratio of nLw 490 : nLw 670 channels in the LaTTE region 04/09/2005
40° 30′
40° 15′
40° 0′
39° 45′
39° 30′
−74° 15′
−74° 0′
−73° 45′
−73° 30′
−73° 15′
40 m
60 m
60 m
15 m
5 m

Fig. 7b.

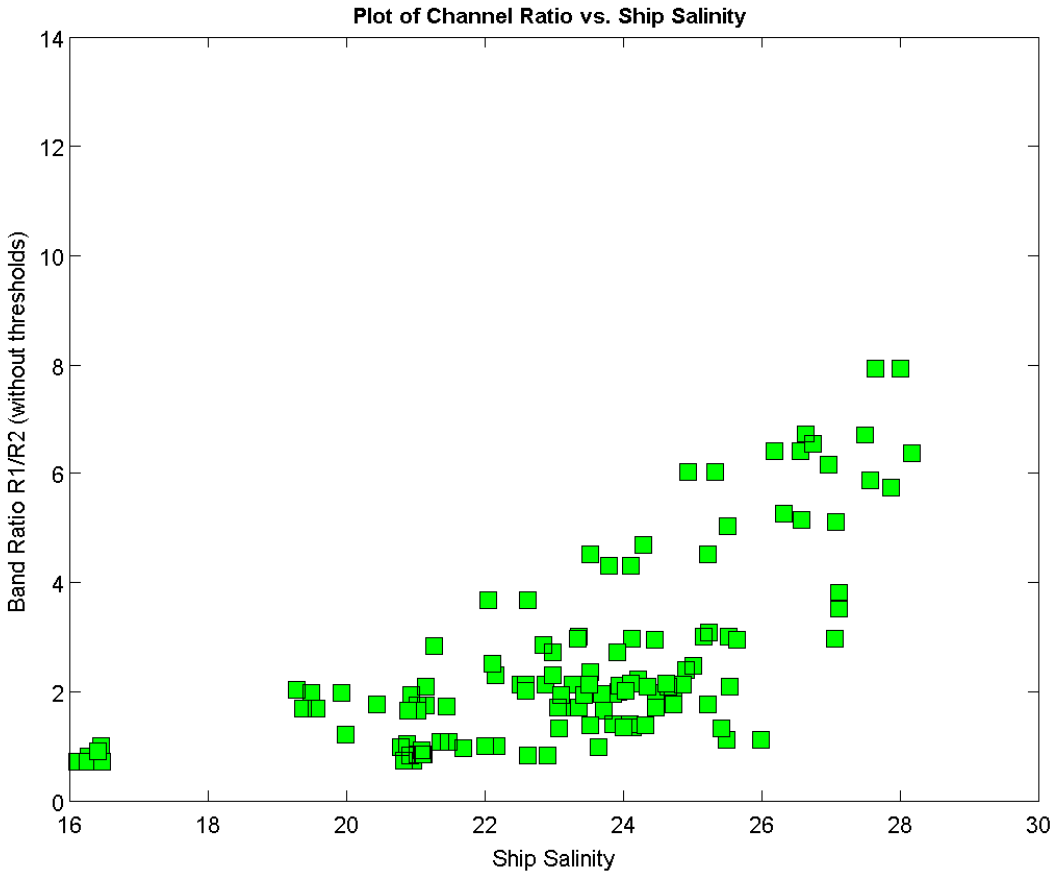
Plot of Channel Ratio vs. Ship Salinity
Band Ratio R1/R2 (without thresholds)
Ship Salinity
0
2
4
6
8
10
12
14
16
18
20
22
24
26
28
30

Fig. 7c.

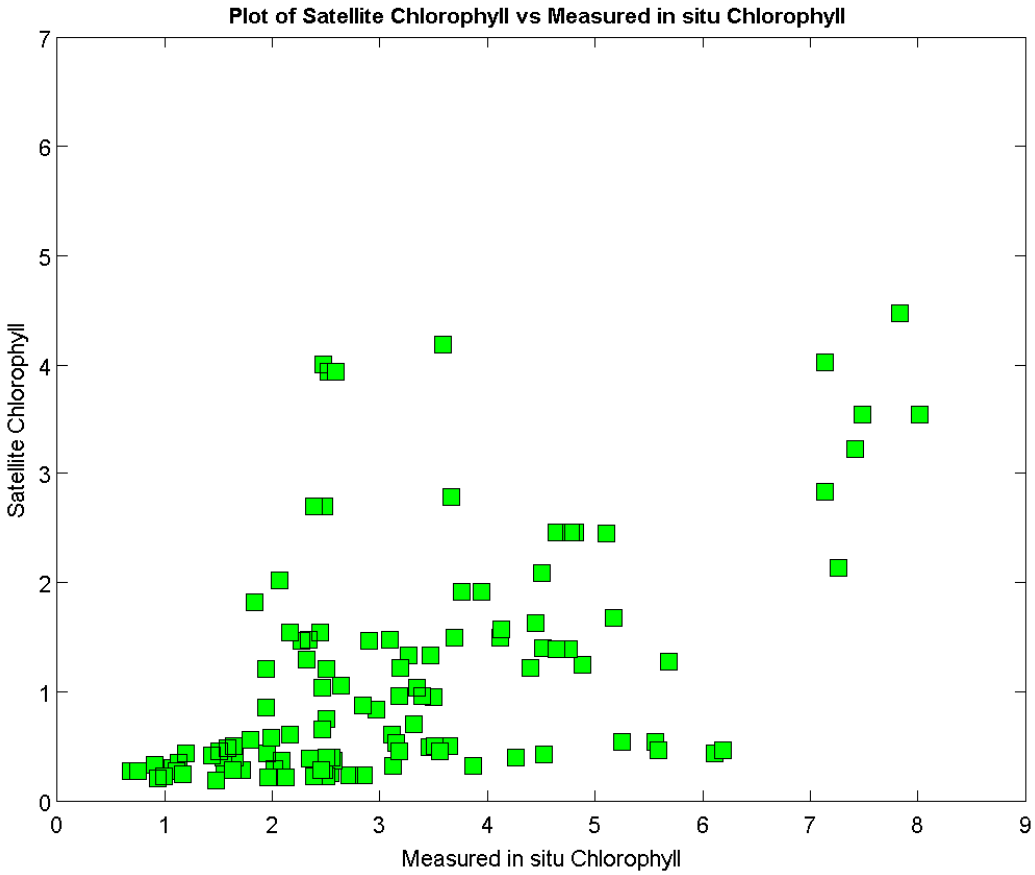

Fig. 7d.

Fig. 7: Water mass algorithm applied with thresholds changed to
a) 25% less and b) 25% more
c) Band ratios vs. ship salinity values; d) Correlation of measured vs. satellite chlorophyll

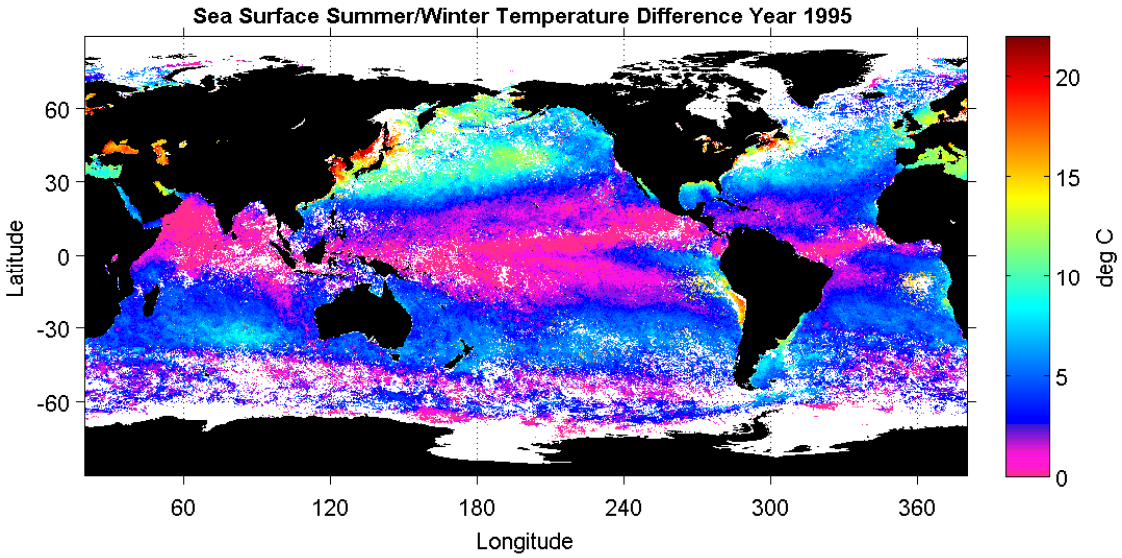
Sea Surface Summer/Winter Temperature Difference Year 1995
Latitude
60
30
0
-30
-60
60
120
180
240
300
360
Longitude
20
15
10
5
0
deg C

Fig. 8a

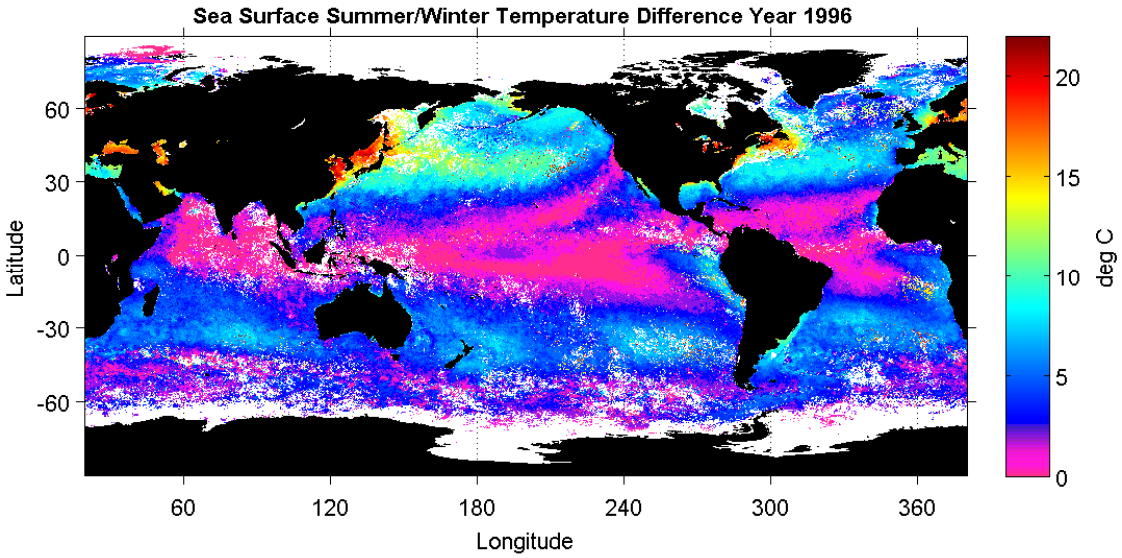
Sea Surface Summer/Winter Temperature Difference Year 1996
Latitude
60
30
0
-30
-60
60
120
180
240
300
360
Longitude
20
15
10
5
0
deg C

Fig. 8b.

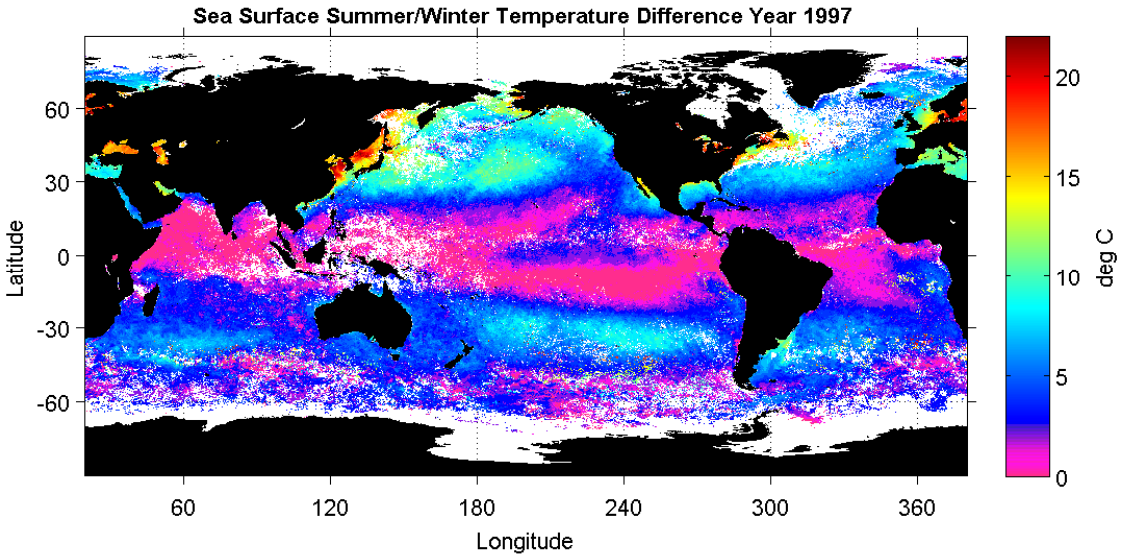
Sea Surface Summer/Winter Temperature Difference Year 1997
Latitude
60
30
0
-30
-60
60
120
180
240
300
360
Longitude
20
15
10
5
0
deg C

Fig. 8c.

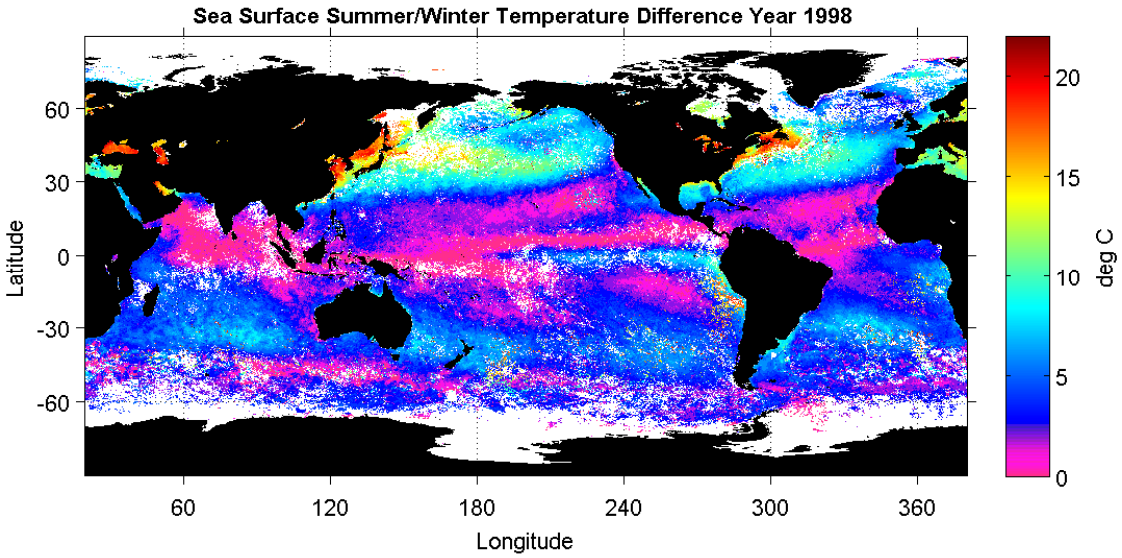
Sea Surface Summer/Winter Temperature Difference Year 1998
Latitude
60
30
0
-30
-60
60
120
180
240
300
360
Longitude
20
15
10
5
0
deg C

Fig. 8d.

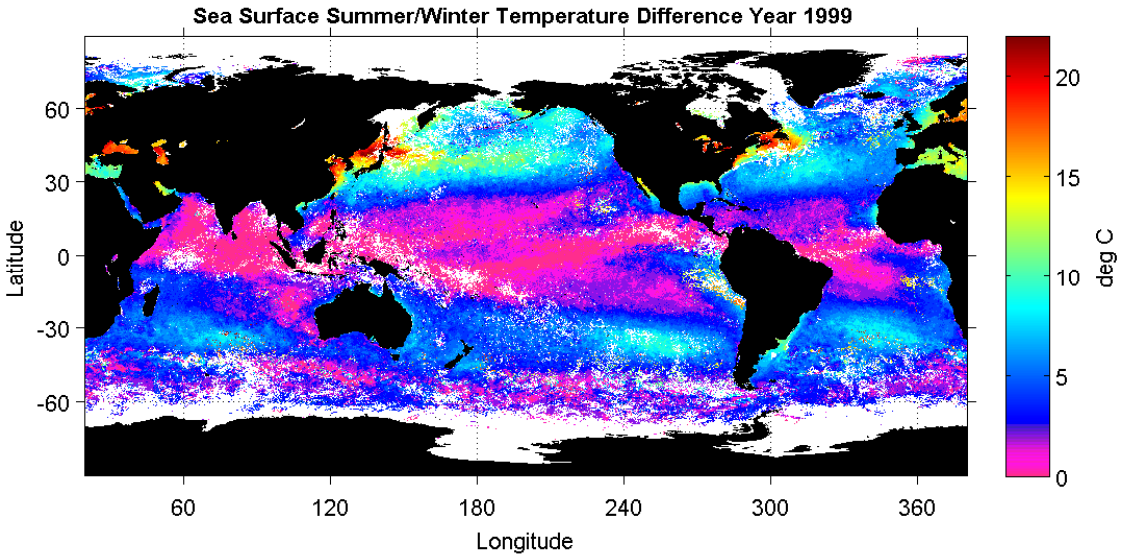
Sea Surface Summer/Winter Temperature Difference Year 1999
Latitude
60
30
0
-30
-60
60
120
180
240
300
360
Longitude
20
15
10
5
0
deg C

Fig. 8e.

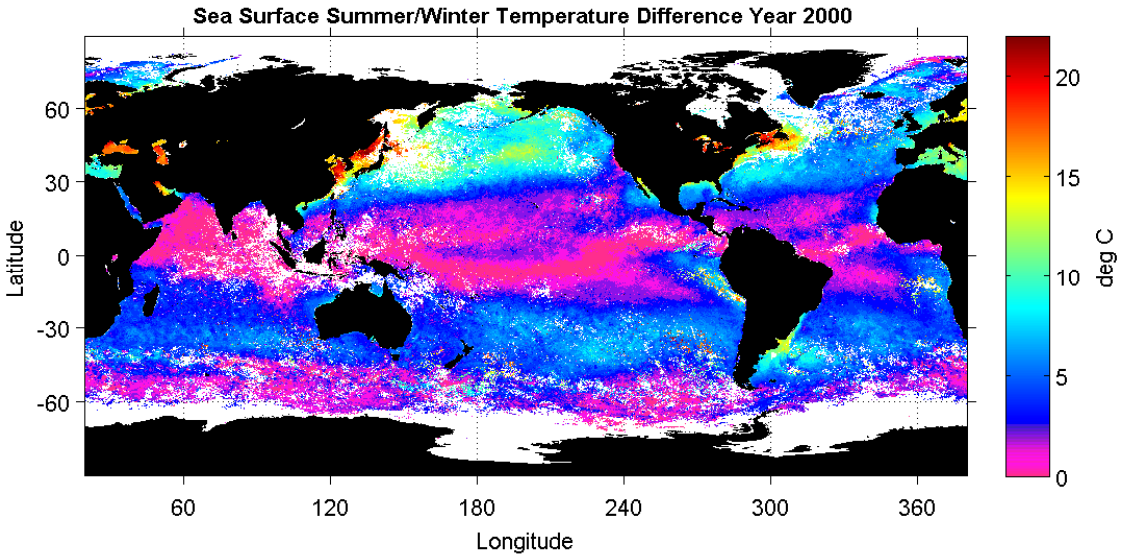
Sea Surface Summer/Winter Temperature Difference Year 2000
Latitude
60
30
0
-30
-60
60
120
180
240
300
360
Longitude
20
15
10
5
0
deg C

Fig. 8f.

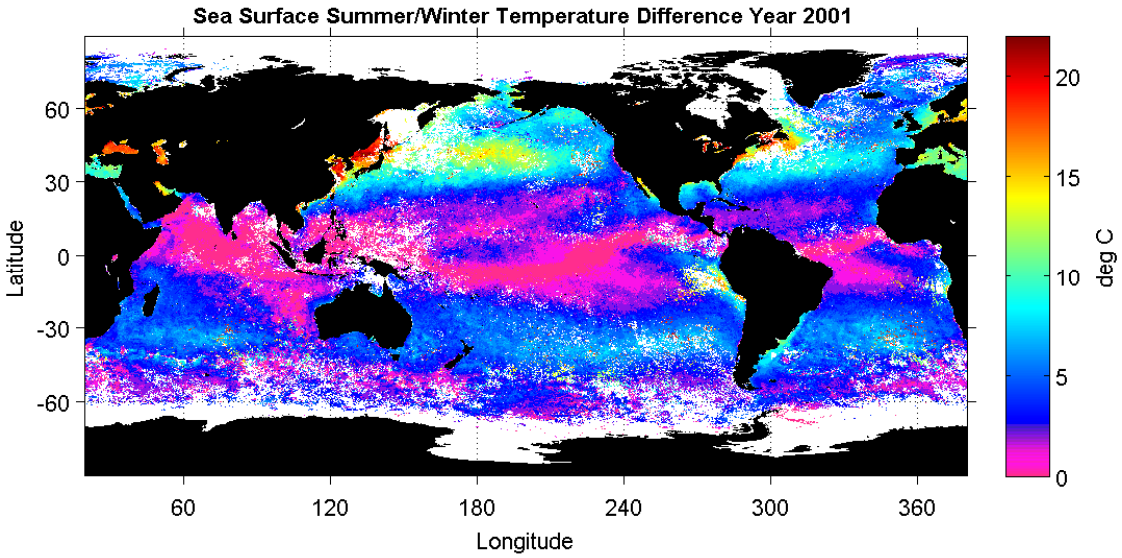
Sea Surface Summer/Winter Temperature Difference Year 2001
Latitude
60
30
0
-30
-60
60
120
180
240
300
360
Longitude
20
15
10
5
0
deg C

Fig. 8g.

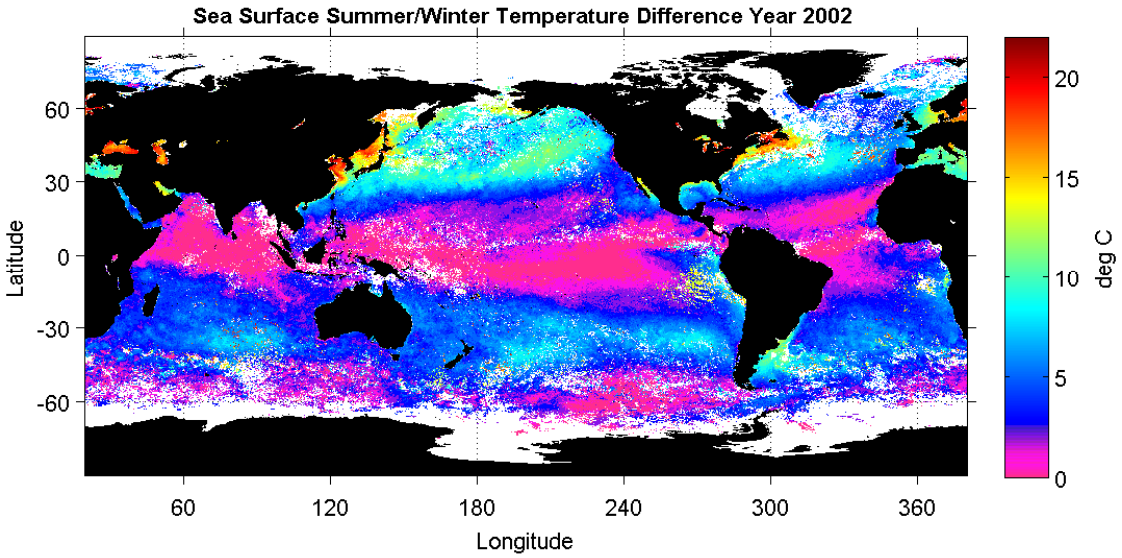
Sea Surface Summer/Winter Temperature Difference Year 2002
Latitude
60
30
0
-30
-60
60
120
180
240
300
360
Longitude
20
15
10
5
0
deg C

Fig. 8h.

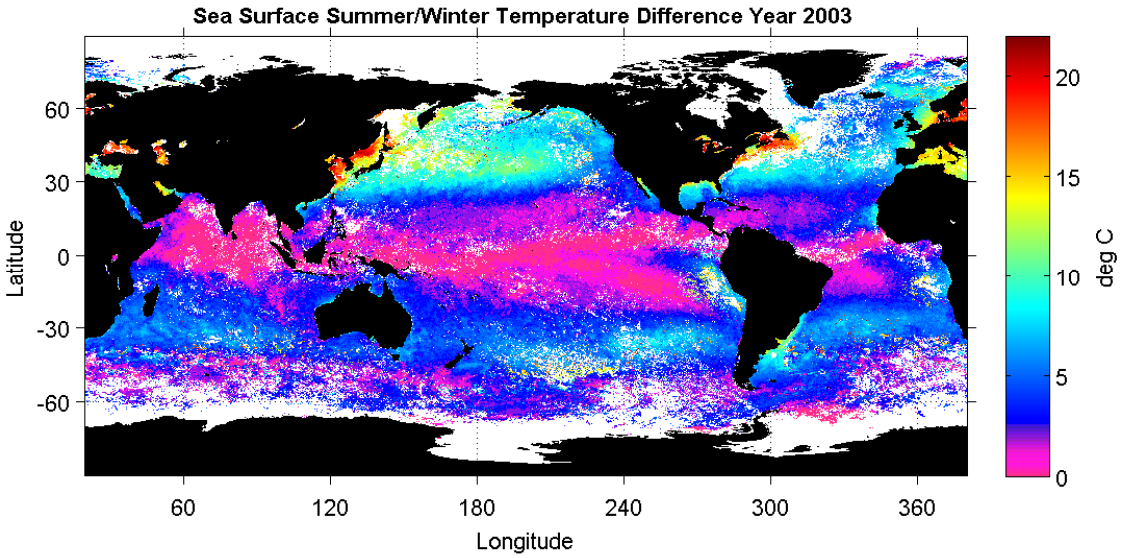
Sea Surface Summer/Winter Temperature Difference Year 2003
Latitude
60
30
0
-30
-60
60
120
180
240
300
360
Longitude
20
15
10
5
0
deg C

Fig. 8i

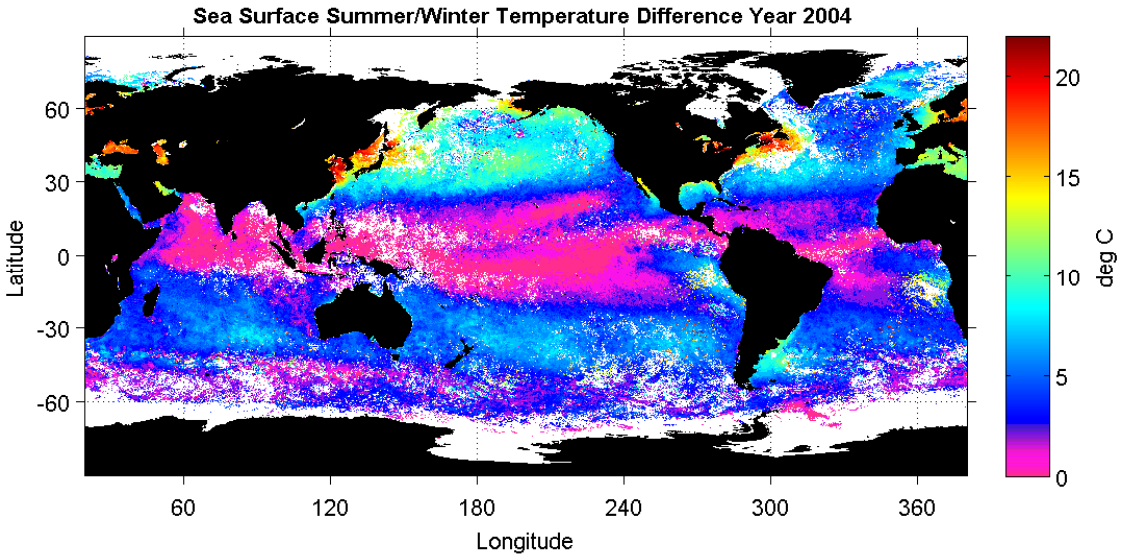
Sea Surface Summer/Winter Temperature Difference Year 2004
Latitude
60
30
0
-30
-60
60
120
180
240
300
360
Longitude
20
15
10
5
0
deg C

Fig. 8j.

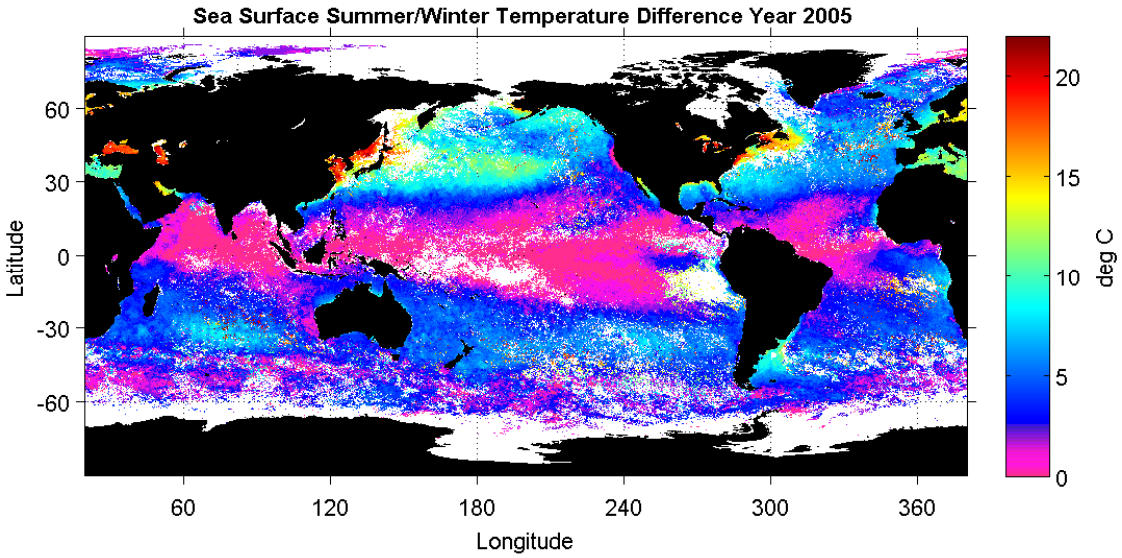

Fig. 8k.

Fig. 8: 11-year global SST summer-winter difference 1995-2005.

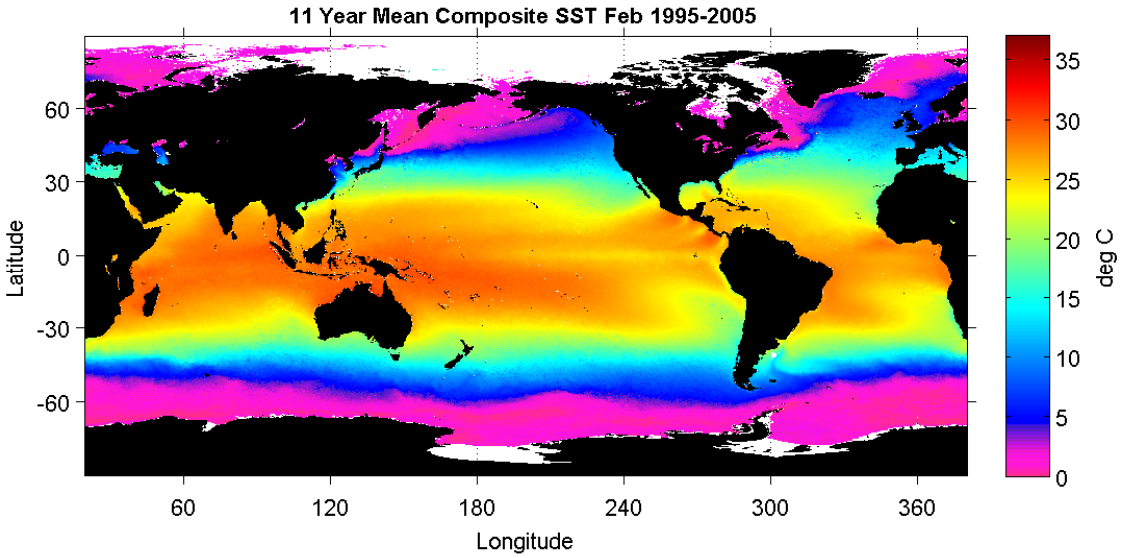
11 Year Mean Composite SST Feb 1995-2005
Latitude
60
30
0
-30
-60
60
120
180
240
300
360
Longitude
35
30
25
20
15
10
5
0
deg C

Fig. 9a.

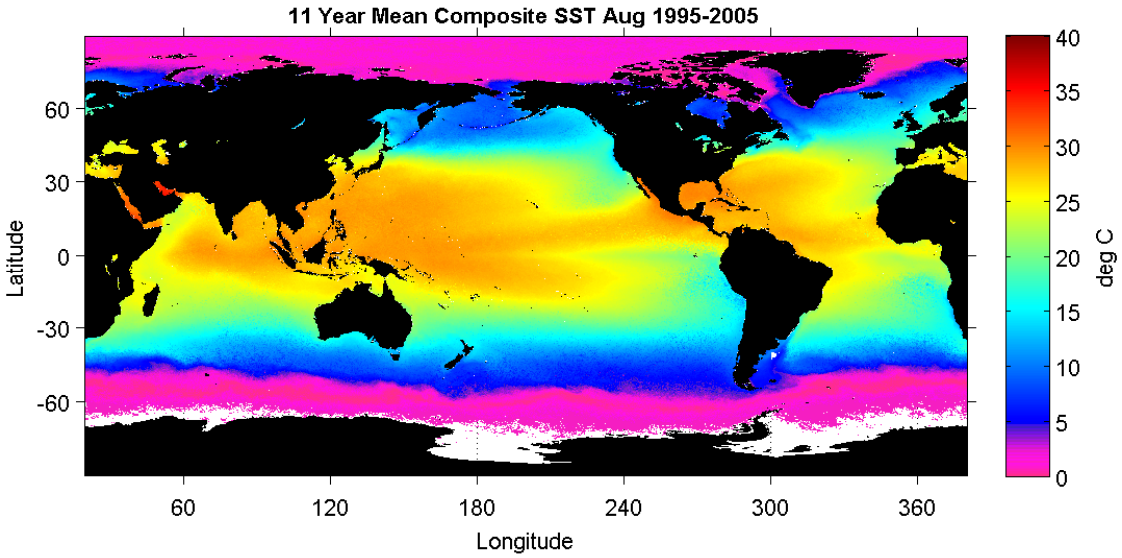
11 Year Mean Composite SST Aug 1995-2005
Latitude
60
30
0
-30
-60
60
120
180
240
300
360
Longitude
40
35
30
25
20
15
10
5
0
deg C

Fig. 9b.

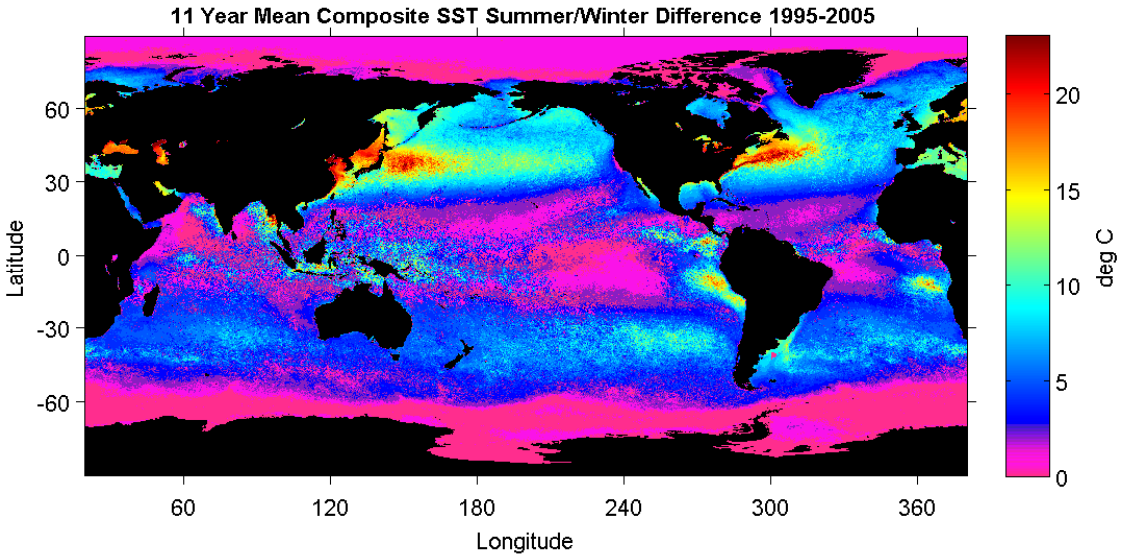

Fig. 9c.

Fig. 9: 11-year mean SST composites:
a) Feb 1995-2005; b) Aug 1995-2005; c) Summer-winter difference

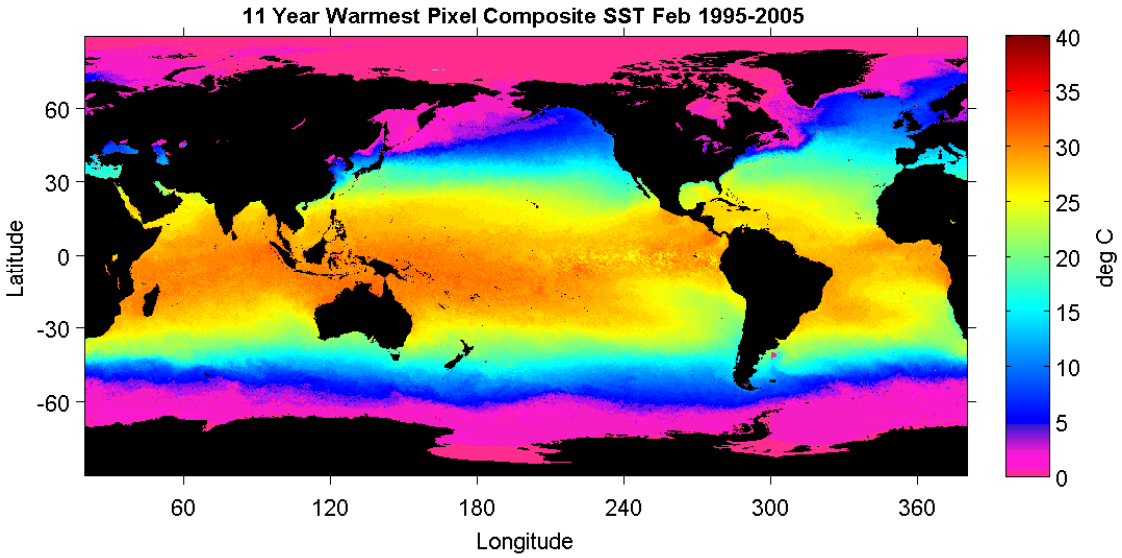
11 Year Warmest Pixel Composite SST Feb 1995-2005
Latitude
60
30
0
-30
-60
60
120
180
240
300
360
Longitude
40
35
30
25
20
15
10
5
0
deg C

Fig. 10a.

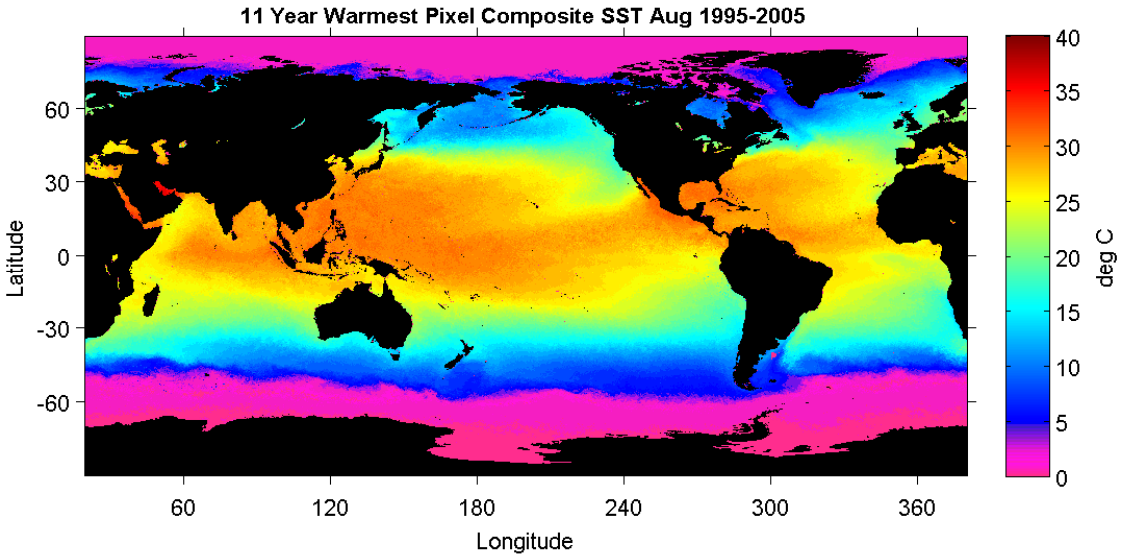
11 Year Warmest Pixel Composite SST Aug 1995-2005
Latitude
60
30
0
-30
-60
60
120
180
240
300
360
Longitude
40
35
30
25
20
15
10
5
0
deg C

Fig. 10b.

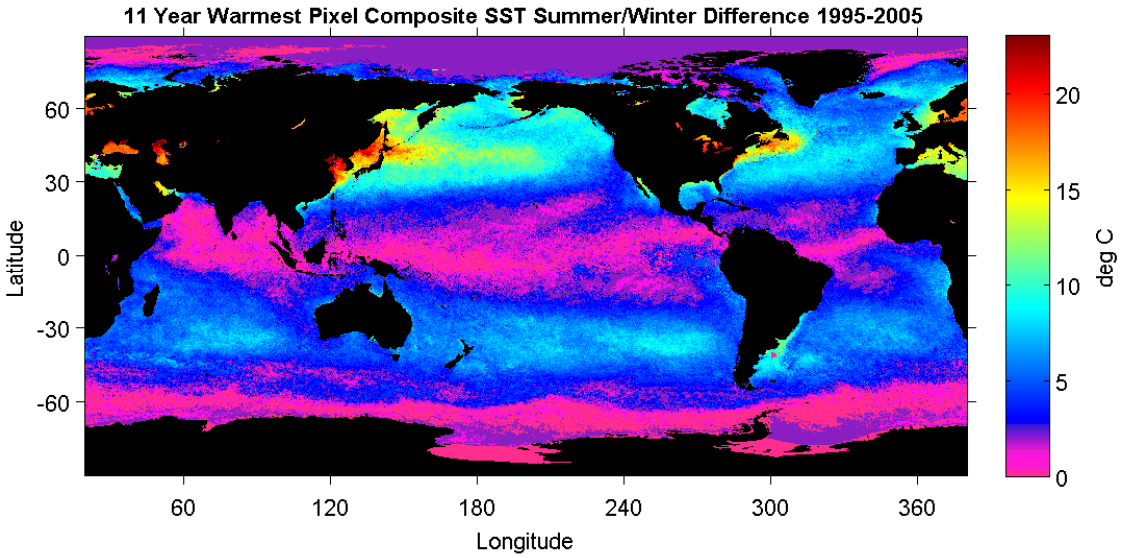

Fig. 10c

Fig. 10: 11- year warmest pixel SST composites:
a) Feb 1995-2005; b) Aug 1995-2005; c) Summer-winter difference

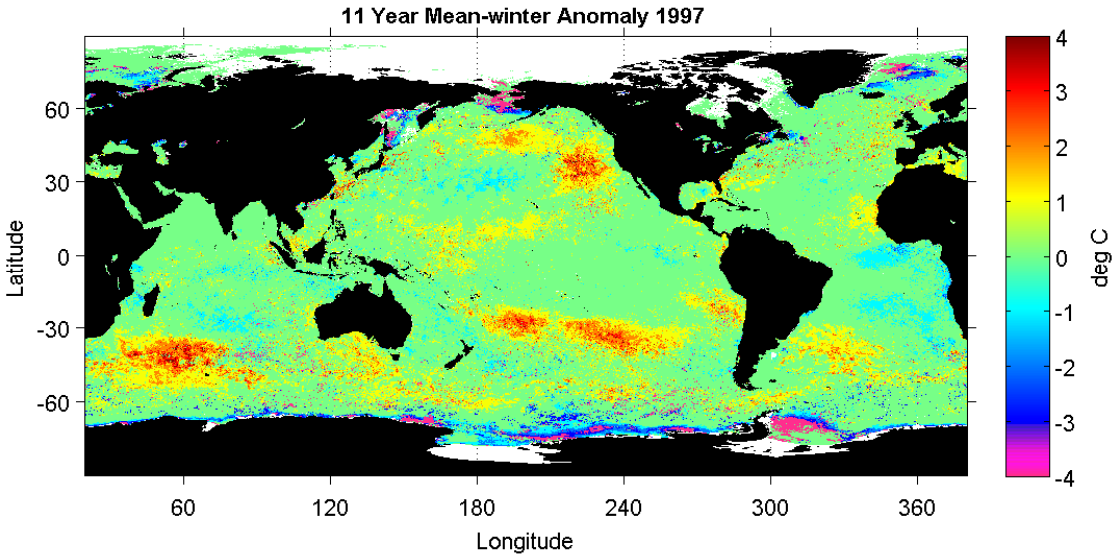
11 Year Mean-winter Anomaly 1997
Latitude
60
30
0
-30
-60
60
120
180
240
300
360
Longitude
4
3
2
1
0
-1
-2
-3
-4
deg C

Fig. 11a.

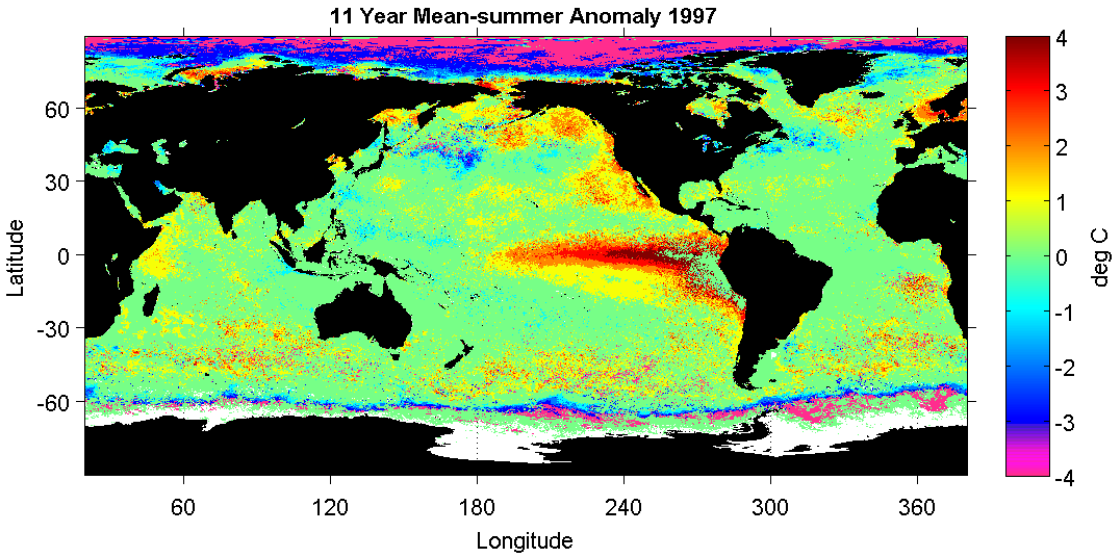
11 Year Mean-summer Anomaly 1997
Latitude
60
30
0
-30
-60
60
120
180
240
300
360
Longitude
4
3
2
1
0
-1
-2
-3
-4
deg C

Fig. 11b.

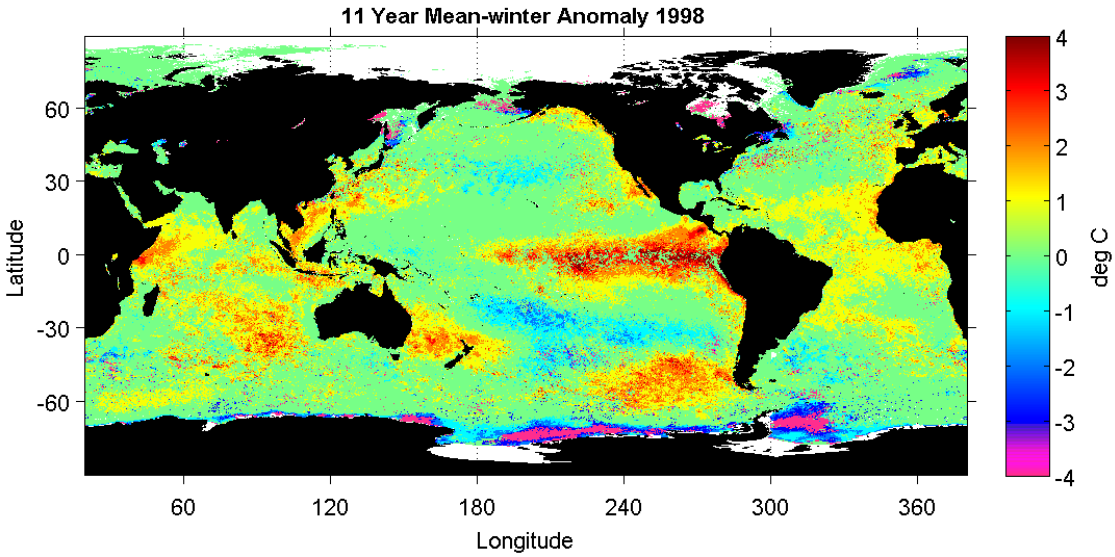
11 Year Mean-winter Anomaly 1998
Latitude
60
30
0
-30
-60
60
120
180
240
300
360
Longitude
4
3
2
1
0
-1
-2
-3
-4
deg C

Fig. 11c.

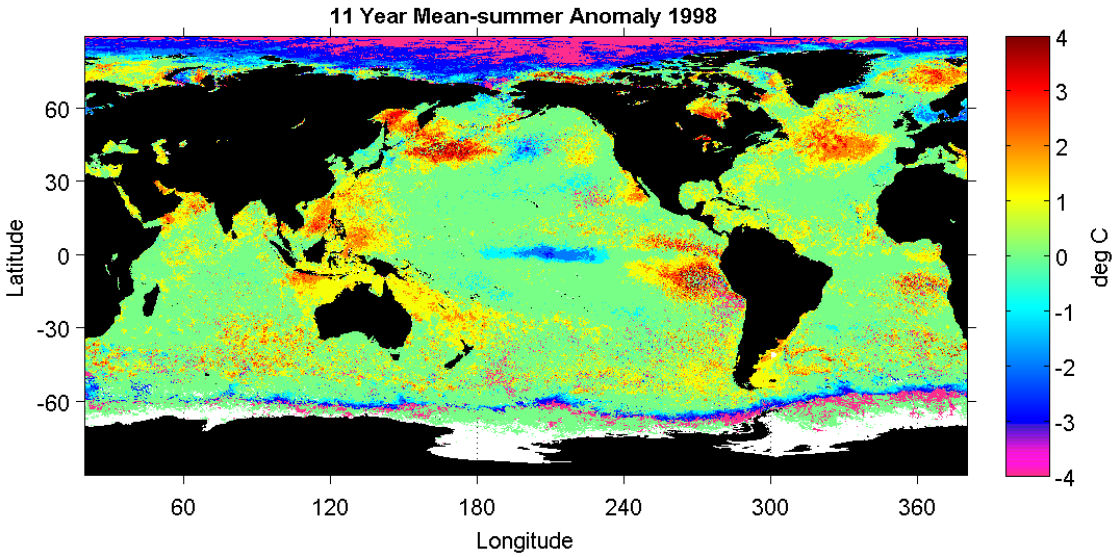

Fig. 11d.

Fig. 11: Mean Anomaly for the years 1997-1998 indicating the onset and end of the massive El Niño of 1997-1998

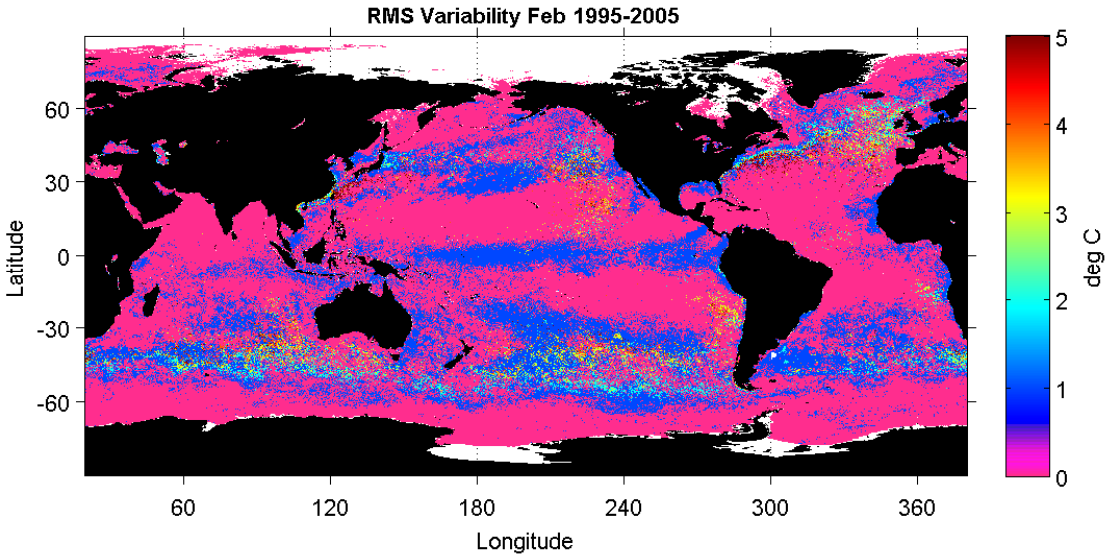
RMS Variability Feb 1995-2005
Latitude
60
30
0
-30
-60
60
120
180
240
300
360
Longitude
5
4
3
2
1
0
deg C

Fig. 12a.

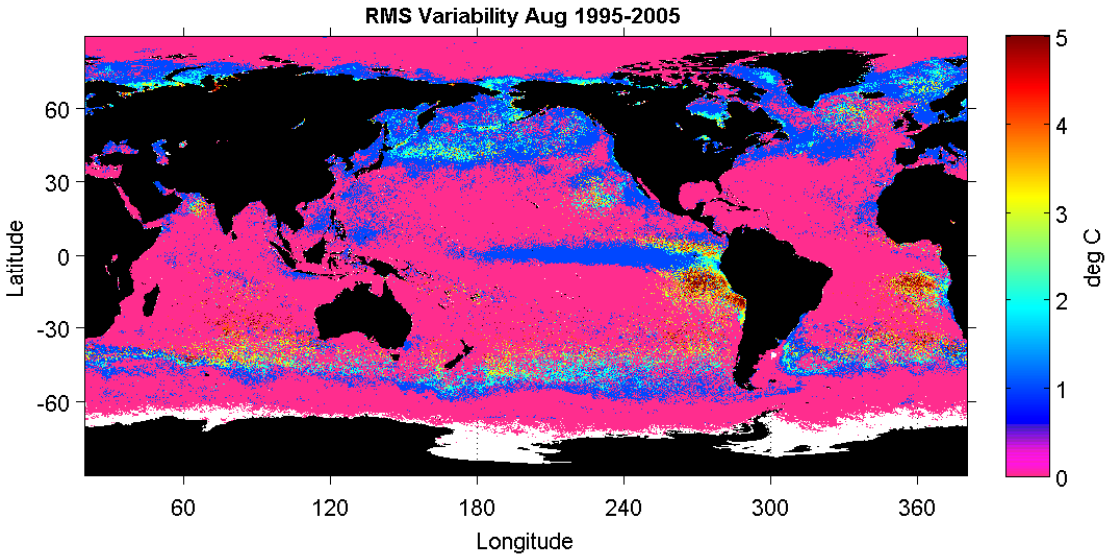

Fig. 12b
Fig. 12: RMS Variability for 1995-2005

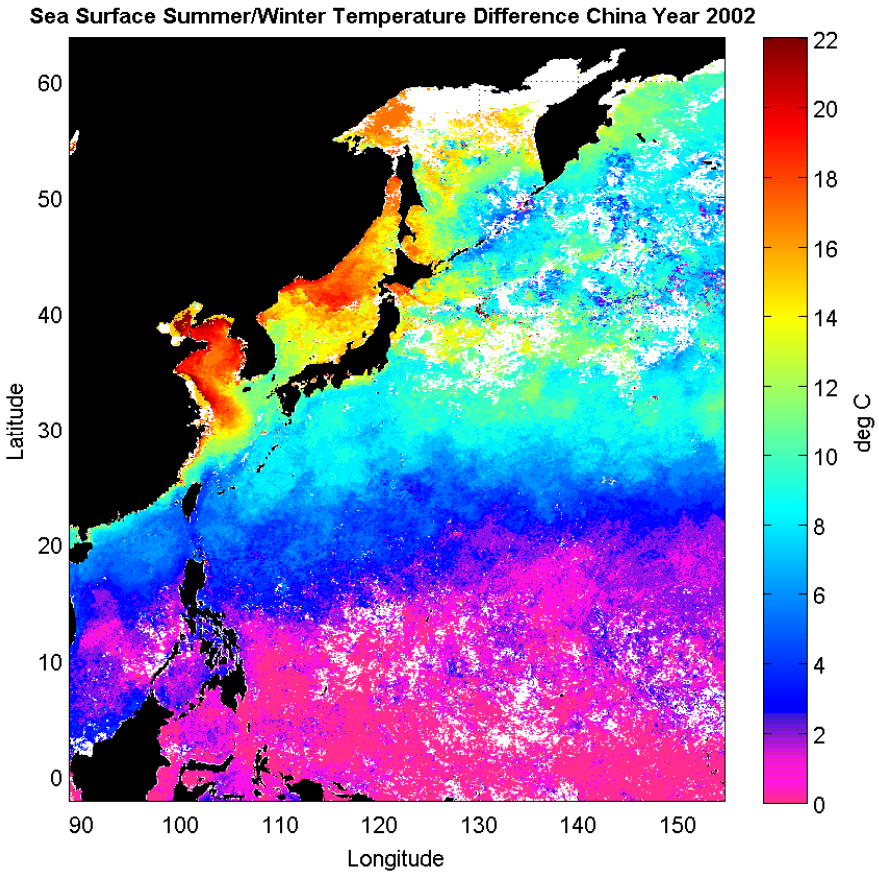
Sea Surface Summer/Winter Temperature Difference China Year 2002
Latitude
Longitude
deg C
60
50
40
30
20
10
0
90
100
110
120
130
140
150
22
20
18
16
14
12
10
8
6
4
2
0

Fig. 13a.

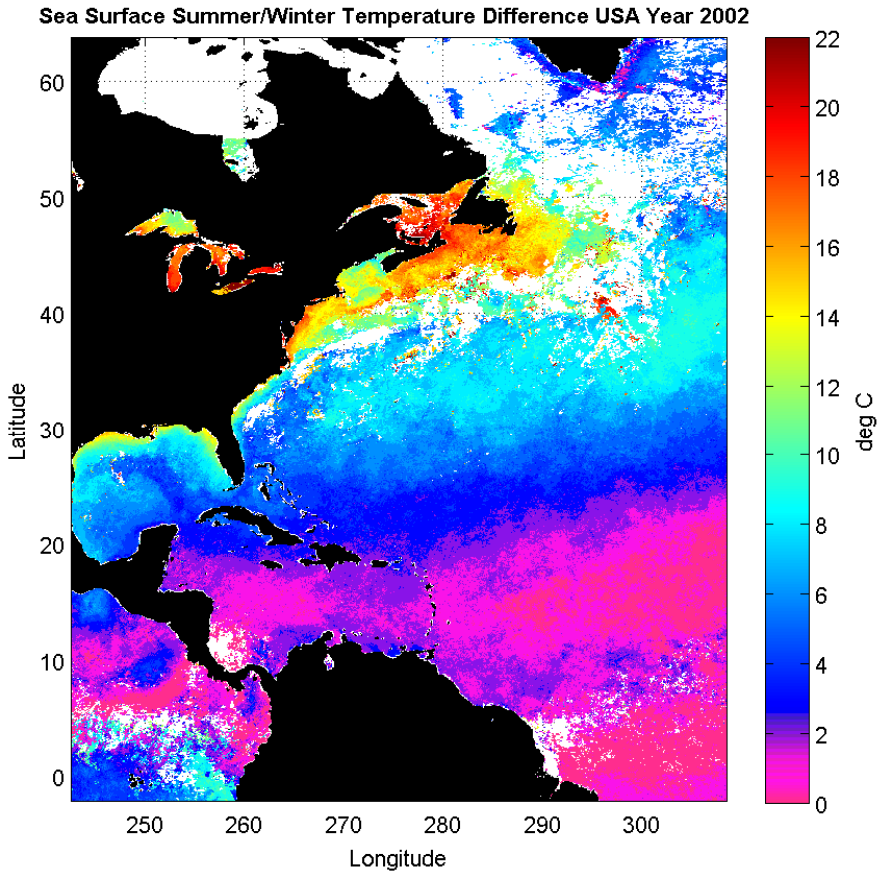

Fig. 13b.

Fig. 13: Zoomed-in plots of the Asian coast and the US east coast for the year 2002 to show the similarity in the two regions. This year's data was used to apply the water mass algorithm to the Asian waters.

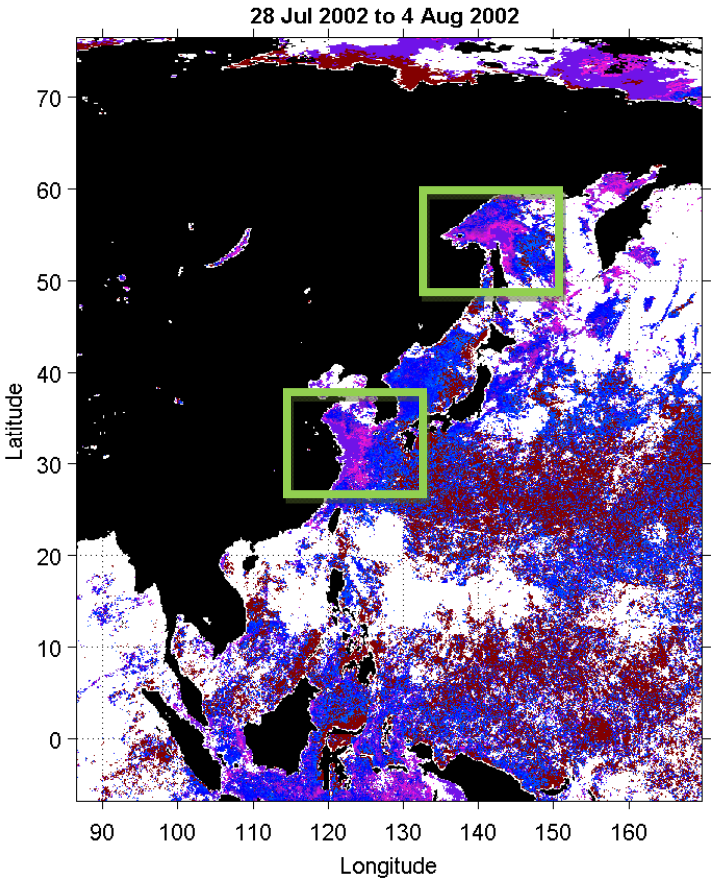
28 Jul 2002 to 4 Aug 2002
70
60
50
40
30
20
10
0
Latitude
90
100
110
120
130
140
150
160
Longitude

Fig. 14a.

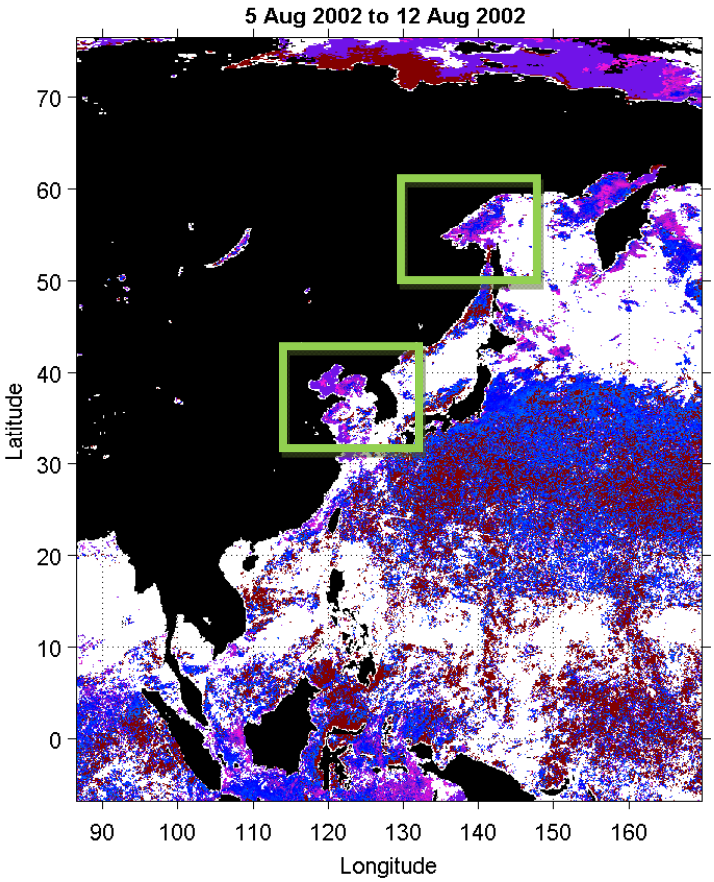
5 Aug 2002 to 12 Aug 2002
Latitude
70
60
50
40
30
20
10
0
90
100
110
120
130
140
150
160
Longitude

Fig. 14b.

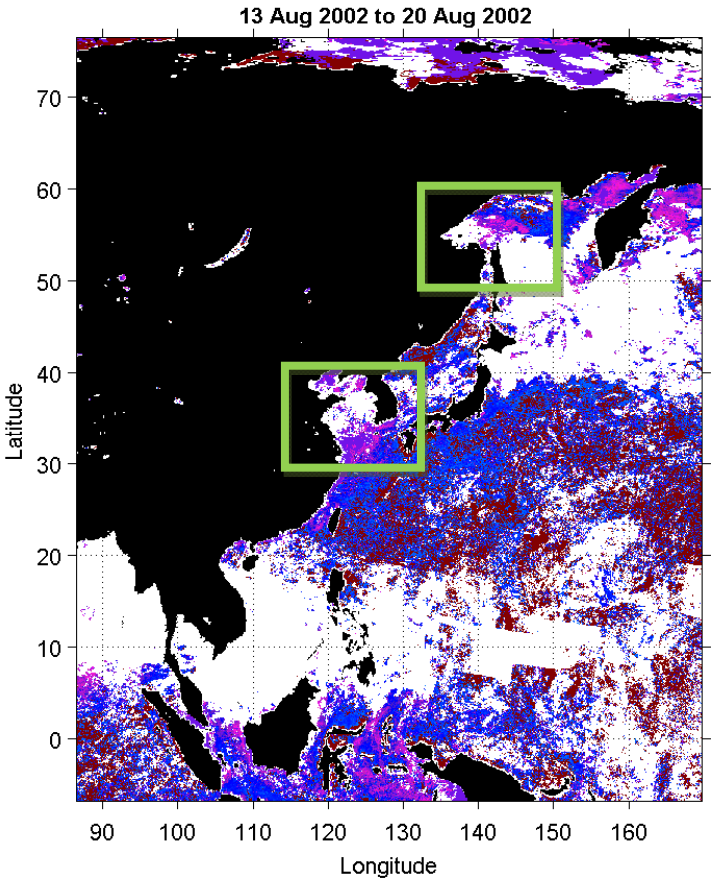
13 Aug 2002 to 20 Aug 2002
Latitude
70
60
50
40
30
20
10
0
90
100
110
120
130
140
150
160
Longitude

Fig. 14c.

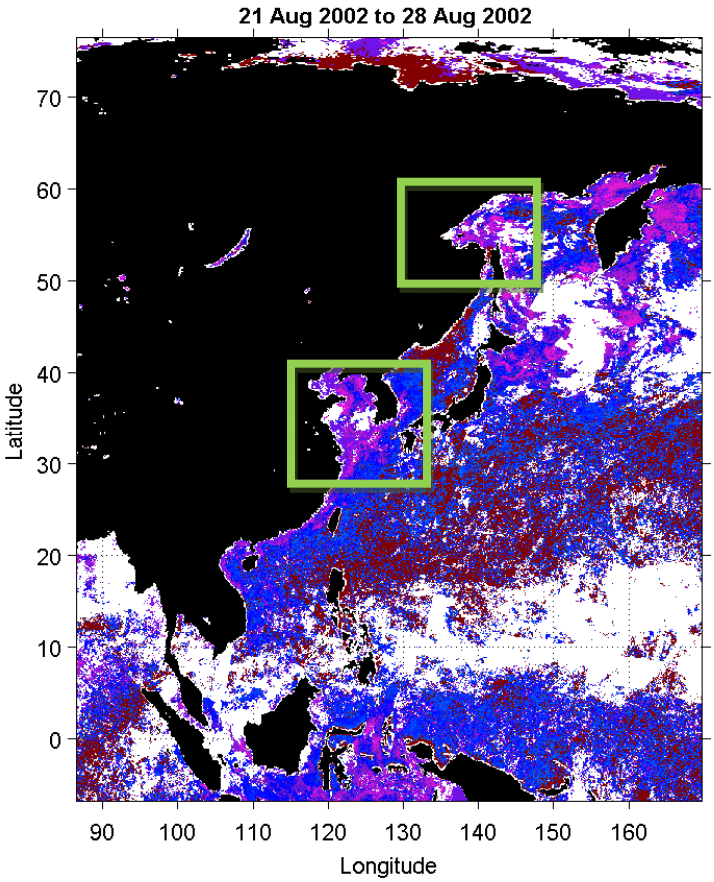
21 Aug 2002 to 28 Aug 2002
Latitude
70
60
50
40
30
20
10
0
90
100
110
120
130
140
150
160
Longitude

Fig. 14d.

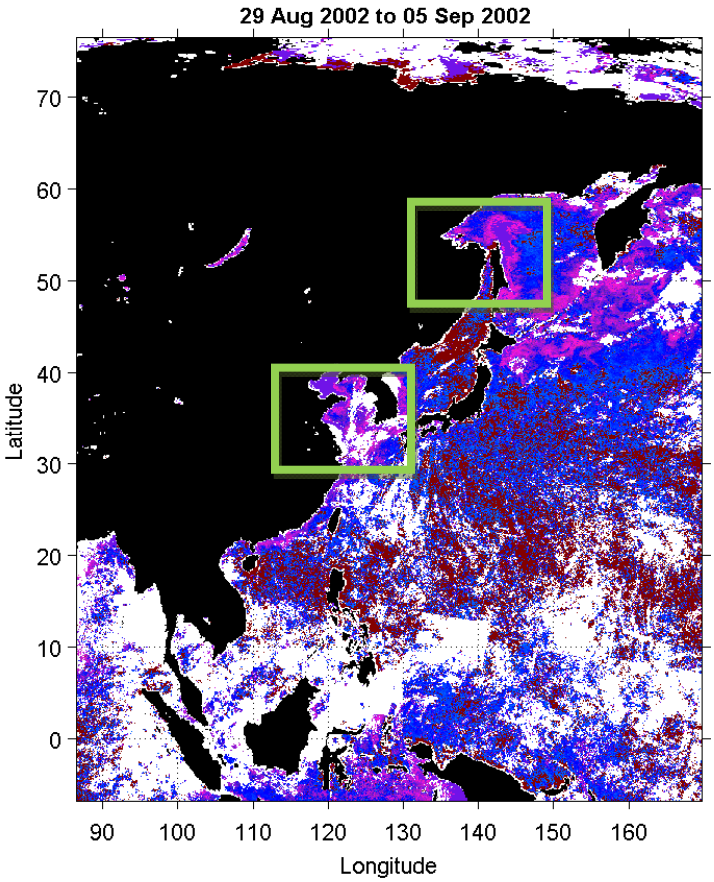

Fig. 14e.

Fig. 14: Water mass tagging applied to the East Asian Coast, Aug 2002.

References

Aiken, J., Moore, G.F., Trees, C.C., Hooker, S.B. & Clark, D.K. 1995, "The SeaWiFS CZCS-type pigment algorithm", *NASA Tech. Memo,* .

Alekseev, A.V., Baklanov, P.J., Arzamastsev, I.S., Blinov, Y.G., Fedorovskii, A.S., Kachur, A.N., Khrapchenkov, F.F., Medvedeva, I.A., Minakir, P.A., Titova, G.D., Vlasov, A.V., Voronov, B.A. & Ishitobi, H. 2006, *Global International Waters Assessment Sea of Okhotsk, GIWA Regional assessment 30,* University of Kalmar on behalf of United Nations Environment Programme.

Alvaina, S., Moulina, C., Dandonneaub, Y. & Bréona, F.M. 2005, "Remote sensing of phytoplankton groups in case 1 waters from global SeaWiFS imagery", *Deep Sea Research Part I: Oceanographic Research Papers,* vol. 52, no. 11, pp. 1989-2004.

Austin, R.W. & Petzold, T.J. 1981, "The determination of the diffuse attenuation coefficient of sea water using the Coastal Zone Color Scanner", *Oceanography from Space,* , pp. 239-256.

Barnard, A.H., Zaneveld, J. Ronald V. & Pegau, W.S. 1999, "In Situ Determination of the Remotely Sensed Reflectance and the Absorption Coefficient: Closure and Inversion", *Applied Optics,* vol. 38, no. 24, pp. 5108-5117.

Barnston, A.G. & Smith, T.M. 1996, "Specification and Prediction of Global Surface Temperature and Precipitation from Global SST Using CCA", *Journal of Climate,* vol. 9, no. 11, pp. 2660-2697.

Bosch, J., Schofield, O., Glenn, S. & Kohut, J.T. 2004, "East coast plumes and blooms: building a chlorophyll budget for the mid-atlantic bight", *OceanOptics XVII,* .

Brown, J.W., Brown, O.B. & Evans, R.H. 1993, "Calibration of advanced very high resolution radiometer infrared channels: A new approach to nonlinear correction", *Journal of Geophysical Research,* vol. 98, no. C10, pp. 18257-18268.

Campbell, J.W. & Esaias, W.E. 1983, "Basis for spectral curvature algorithms in remote sensing of chlorophyll", *Applied Optics,* vol. 22, no. 7, pp. 1084.

Carder, K.L., Chen, F.R., Lee, Z.P., Hawes, S.K. & Kamykowski, D. 1999, "Semianalytic Moderate-Resolution Imaging Spectrometer algorithms for chlorophyll *a* and absorption with bio-optical domains based on nitrate-depletion temperatures", *Journal of Geophysical Research,* vol. 104, no. C3, pp. 5403-5421.

Clark, D.K., Baker, E.T. & Strong, A.E. 1980, "Upwelled spectral radiance distribution in relation to particulate matter in sea water", *Boundary-Layer Meteorology,* vol. 18, no. 3, pp. 287-298.

Dulepova, E. & Radchenko, V. "Okhotsk Sea" in *Marine Ecosystems of the North Pacific* PICES Special Publication 1, .

Eppley, R.W., Stewart, E., Abbott, M.R. & Heyman, U. 1985, "Estimating ocean primary production from satellite chlorophyll. Introduction to regional differences and statistics for the Southern California Bight", *Journal of Plankton Research,* vol. 7, no. 1, pp. 57-70.

Feldman, G. 2008, *, OceanColor Web* [Homepage of NASA], [Online]. Available: http://oceancolor.gsfc.nasa.gov/ [2008, .

Glenn, S.M., Crowley, M.F., Haidvogel, D.B. & Song, Y.T. 1996, "Underwater observatory captures coastal upwelling events off New Jersey", *Eos, Transactions American Geophysical Union,* vol. 77, no. 25, pp. 233-233.

Glenn, S., Arnone, R., Bergmann, T., Bissett, W.P., Crowley, M., Cullen, J., Gryzmski, J., Haidvogel, D., Kohut, J. & Moline, M. 2004, "Biogeochemical impact of summertime coastal upwelling on the New Jersey Shelf", *Journal of Geophysical Research,* vol. 109, pp. C12S02.

Gordon, H.R., Clark, D.K., Brown, J.W., Brown, O.B., Evans, R.H. & Broenkow, W.W. 1983, "Phytoplankton pigment concentrations in the Middle Atlantic Bight: comparison of ship determinations and CZCS estimates", *Applied Optics,* vol. 22, no. 1, pp. 20.

Gordon, H.R. & Wang, M. 1993, "Retrieval of water-leaving radiance and aerosol optical thickness over the oceans with SeaWiFS: a preliminary algorithm", *Applied Optics,* vol. 33, no. 3, pp. 443-452.

Harada, N., Ahagon, N., Sakamoto, T., Uchida, M., Ikehara, M. & Shibata, Y. 2006, "Okhotsk Sea MD01-2412 Alkenone Data and SST Reconstruction", *IGBP PAGES/World Data Center for Paleoclimatology, .*

Hovis, W.A., Clark, D.K., Anderson, F., Austin, R.W., Wilson, W.H., Baker, E.T., Ball, D., Gordon, H.R., Mueller, J.L., El-Sayed, S.Z., Sturm, B., Wrigley, R.C. &

Yentsch, C.S. 1980, "Nimbus-7 Coastal Zone Color Scanner: System Description and Initial Imagery", *Science,* vol. 210, no. 4465, pp. 60-63.

Iwasaki, S., Kubota, M. & Tomita, H. 2006, "Comparison of two global SST datasets", *1st Joint GOSUD/SAMOS Workshop*.

Jerlov, N.G. 1951, "Optical studies of ocean water", *Rept. Swed. Deep–Sea Exped,* .

Johnson, D.R., Miller, J. & Schofield, O. 2003, "Dynamics and optics of the Hudson River outflow plume", *Journal of Geophysical Research,* vol. 108, no. C10, pp. 3323.

Kaplan, A., Cane, M.A., Kushnir, Y., Clement, A.C., Blumenthal, M.B. & Rajagopalan, B. 1998, "Analyses of global sea surface temperature 1856-1991", *Journal of Geophysical Research,* vol. 103, no. C9, pp. 18567-18590.

Kidder, S.Q. & Vonder Haar, T.H. 1995, *Satellite Meteorology: An Introduction,* 1st edn, Academic Press.

Kilpatrick, K.A., Podesta, G.P. & Evans, R. 2001, "Overview of the NOAA/NASA advanced very high resolution radiometer Pathfinder algorithm for sea surface temperature and associated matchup database", *Journal of Geophysical Research,* vol. 106, no. C5, pp. 9179-97.

Kirk, J.T.O. 1994, *Light and Photosynthesis in Aquatic Ecosystems,* 1st edn, Cambridge University Press.

Lee, Z. & Carder, K.L. 2000, "Band-ratio or spectral-curvature algorithms for satellite remote sensing?", *Applied Optics,* vol. 39, no. 24, pp. 4377-4380.

Lee, Z.P., Carder, K., Steward, R., Peacock, T., Davis, C. & Patch, J. 1998, "An empirical algorithm for light absorption by ocean water based on color", *Journal of Geophysical Research,* vol. 103, no. C12, pp. 27967-27978.

Levinton, J.S. & Waldman, J.R. 2006, *The Hudson River Estuary,* 1st edn, Cambridge University Press.

Limburg, K.E., Moran, M.A. & McDowell, W.H. 1986, *The Hudson River Ecosystem,* Springer.

MacQueen, J.B. 1967, "Some methods of classification and analysis of multivariate observations", *Proceedings of 5-th Berkeley Symposium on Mathematical Statistics and Probability,* vol. 1, pp. 281-297.

Malone, T.C. 1976, "Phytoplankton Productivity in the Apex of the New York Bight: Environmental Regulation of Productivity/Chlorophyll A", *Proceedings of symposium:'Middle Atlantic Continental Shelf and the New York Bight '*, pp. 260.

McClain, E.P., Pichel, W.G. & Walton, C.C. 1985, "Comparative performance of AVHRR-based multichannel sea surface temperatures", *Journal of Geophysical Research,* vol. 90, no. C14, pp. 11587-11601.

McClain, C., Feldman, G. & Hooker, S.B. 2004, "An overview of the SeaWiFS project and strategies for producing a climate research quality global ocean bio-optical time series", *Deep Sea Research Part II: Topical Studies in Oceanography,* vol. 51, no. 1-3, pp. 5-42.

McPhaden, M.J. 1999, "Genesis and Evolution of the 1997-98 El Niño", *Science,* vol. 283, no. 5404, pp. 950-954.

Morel, A. 1973, "Diffusion de la lumiere par les eaux de mer. Résultats expérimentaux et approche théorique", *Optics of the Sea,* vol. 61.

Morel, A. & Bricaud, A. 1981, "Theoretical results concerning light absorption in a discrete medium, and application to specific absorption of phytoplankton", *Deep Sea Research Part A. Oceanographic Research Papers,* vol. 28, no. 11, pp. 1375-1393.

Morel, A. & Prieur, L. 1977, "Analysis of Variations in Ocean Color", *Limnology and Oceanography,* vol. 22, no. 4, pp. 709-722.

Mueter, F.J., Broms, C., Drinkwater, K.F., Friedland, K., Hare, J., Hunt Jr., G., Melle, W. & Taylor, M. 2007, *Comparison of 4 Northern Hemisphere regions: Physical oceanographic responses to recent climate variability*.

NOAA 2008, , *Advanced Very High Resolution Radiometer - AVHRR* [Homepage of NOAA Satellite and Information Service], [Online]. Available: http://noaasis.noaa.gov/NOAASIS/ml/avhrr.html [2008, .

NOAA 2003, , *Large Marine Ecosystems of the World* [Homepage of NOAA], [Online]. Available: http://na.nefsc.noaa.gov/lme/ [2008, .

O'Reilly, J.E. & Busch, D.A. 1984, "Phytoplankton primary production on the northwestern Atlantic shelf", *Rapp. P.-v. Reun. Cons. Int. Explor. Mer,* vol. 183, no. 0, pp. 255-268.

Oliver, M., Glenn, S., Kohut, J.T., Irwin, A.J., Schofield, O., Moline, M.A. & Bissett, P.W. 2004, "Bioinformatic approaches for objective detection of water masses on continental shelves", *Journal of Geophysical Research,* vol. 109, no. C07S04.

Oracle Inc 2005, , *Spatial Analysis and Mining* [Homepage of Oracle], [Online]. Available: http://youngcow.net/doc/oracle10g/appdev.102/b14255/sdo_sam_concepts.htm#CIHHBIID [2008, .

O'Reilly, J.E., Maritorena, S., Mitchell, B.G., Siegel, D.A., Carder, K.L., Garver, S.A., Kahru, M. & McClain, C. 1998, "Ocean color chlorophyll algorithms for SeaWiFS", *Journal of Geophysical Research,* vol. 103, no. C11, pp. 937-953.

Reynolds, R.W. 1988, "A Real-Time Global Sea Surface Temperature Analysis", *Journal of Climate,* vol. 1, no. 1, pp. 75-87.

Reynolds, R.W. & Smith, T.M. 1995, "A High-Resolution Global Sea Surface Temperature Climatology", *Journal of Climate,* vol. 8, no. 6, pp. 1571-1583.

Roesler, C.S., Perry, M.J. & Carder, K.L. 1989, "Modeling in situ phytoplankton absorption from total absorption spectra in productive inland marine waters", *Limnology and Oceanography,* vol. 34, no. 15, pp. 10-11.

Roesler, C.S. & Perry, M.J. 1995, "In situ phytoplankton absorption, fluorescence emission, and particulate backscattering spectra determined from reflectance", *Journal of Geophysical Research,* vol. 100, no. C7, pp. 279-294.

Roesler, C.S., Perry, M.J. & Carder, K.L. 1989, "Modeling in Situ Phytoplankton Absorption from Total Absorption Spectra in Productive Inland Marine Waters", *Limnology and Oceanography,* vol. 34, no. 8, pp. 1510-1523.

Ryan, J.P., Yoder, J.A. & Cornillon, P.C. 1999, "Enhanced Chlorophyll at the Shelfbreak of the Mid-Atlantic Bight and Georges Bank during the Spring Transition", *Limnology and Oceanography,* vol. 44, no. 1, pp. 1-11.

Schofield, O., Arnone, R.A., Bissett, P.W., Dickey, T.D., Davis, C.O., Finkel, Z., Oliver, M. & Moline, M.A. 2004a, "Watercolors in Coastal Zone", *Oceanography,* vol. 12, no. 2, pp. 24-31.

Schofield, O., Bosch, J., Dickey, T.D., Kohut, J.T., Bowers, L., Chant, R., Haldemann, C., Kerfoot, J., Mudgal, C., Oliver, M., Roarty, H., Romana, E., Crowley, M., Barrick, D. & Jones, C. 2004b, "The Expanding Role of Ocean Color & Optics in the Changing Field of Operational Oceanography", *Oceanography,* vol. 107, pp. 86-95.

Siegel, D.A., Doney, S.C. & Yoder, J.A. 2002, "The North Atlantic Spring Phytoplankton Bloom and Sverdrup's Critical Depth Hypothesis", *Science,* vol. 296, no. 5568, pp. 730-733.

Stowe, L.L., McClain, E.P., Carey, R., Pellegrino, P., Gutman, G.G., Davis, P., Long, C. & Hart, S. 1991, "Global distribution of cloud cover derived from NOAA/AVHRR operational satellite data", *Advances in Space Research,* vol. 11, no. 3, pp. 51-54.

Teng, S.K., Yu, H., Tang, Y., Tong, L., Choi, C.I., Kang, D., Liu, H., Chun, Y., Juliano, R.O., Rautalahti-Miettinen, E. & Daler, D. 2005, "Yellow Sea – GIWA Regional assessment 34", *Global International Waters Assessment Yellow Sea, GIWA Regional assessment 34,* , pp. 1-114.

Terazaki, M. 1999, "The Sea of Japan Large Marine Ecosystem" in *The Large Marine Ecosystems (LMEs) of the Pacific Rim*, eds. Q. Tang & K. Sherman, Blackwell Science, , pp. 199-220.

The HDF Group 2008, , *The HDF Group*. Available: http://hdfgroup.org/ [2008, .

USGS 2006, , *Advanced Very High Resolution Radiometer (AVHRR)* [Homepage of U.S. Geological Survey], [Online]. Available: http://edc.usgs.gov/guides/avhrr.html#avhrr3 [2008, .

Vazquez, J. 2004, , *AVHRR Oceans Pathfinder Sea Surface Temperature Data Sets* [Homepage of Physical Oceanography Distributed Active Archive Center], [Online]. Available: ftp://podaac.jpl.nasa.gov/pub/documents/dataset_docs/avhrr_pathfinder_sst_v5.html#7 [2008, .

Yentsch, C.S. 1984, "Remote Assessment of Ocean Color for Interpretation of Satellite Visible Imagery: A Review. Lecture Notes on Coastal and Estuarine Studies", *The Quarterly Review of biology,* vol. 59, no. 3, pp. 348.